

THE LOW-ENERGY NEUTRAL ATOM IMAGER FOR IMAGE

T. E. MOORE¹, D. J. CHORNAY¹, M. R. COLLIER¹, F. A. HERRERO¹, J. JOHNSON¹,
M. A. JOHNSON¹, J. W. KELLER¹, J. F. LAUDADIO¹, J. F. LOBELL¹,
K. W. OGILVIE¹, P. ROZMARYNOWSKI¹, S. A. FUSELIER², A. G. GHIEMMETTI²,
E. HERTZBERG², D. C. HAMILTON³, R. LUNDGREN³, P. WILSON³, P. WALPOLE³,
T. M. STEPHEN⁴, B. L. PEKO⁴, B. VAN ZYL⁴, P. WURZ⁵, J. M. QUINN⁶ and
G. R. WILSON⁷

¹*NASA Goddard Space Flight Center, Greenbelt, MD 20771, U.S.A.*
(*thomas.e.moore@gssc.nasa.gov*)

²*Lockheed Martin Advanced Technology Center, Palo Alto, CA 94304, U.S.A.*

³*University Of Maryland, College Park, MD 20742, U.S.A.*

⁴*University Of Denver, Denver, CO 80208, U.S.A.*

⁵*University Of Bern, Bern, CH-301, Switzerland*

⁶*University Of New Hampshire, Durham, NH 03824, U.S.A.*

⁷*Mission Research Corp., Nashua, NH 03062, U.S.A.*

(Received May 10, 1999)

Abstract. The 'Imager for Magnetosphere-to-Aurora Global Exploration' (IMAGE) will be launched early in the year 2000. It will be the first mission dedicated to imaging, with the capability to determine how the magnetosphere changes globally in response to solar storm effects in the solar wind, on time scales as short as a few minutes. The low energy neutral atom (LENA) imager uses a new atom-to-negative ion surface conversion technology to image the neutral atom flux and measure its composition (H and O) and energy distribution (10 to 750 eV). LENA uses electrostatic optics techniques for energy (per charge) discrimination and carbon foil time-of-flight techniques for mass discrimination. It has a $90^\circ \times 8^\circ$ field-of-view in 12 pixels, each nominally $8^\circ \times 8^\circ$. Spacecraft spin provides a total field-of-view of $90^\circ \times 360^\circ$, comprised of 12×45 pixels. LENA is designed to image fast neutral atom fluxes in its energy range, emitted by auroral ionospheres or the sun, or penetrating from the interstellar medium. It will thereby determine how superthermal plasma heating is distributed in space, how and why it varies on short time scales, and how this heating is driven by solar activity as reflected in solar wind conditions.

1. Introduction

The low-energy neutral atom (LENA) Imager represents a fundamentally new neutral atom imaging technology, designed for the lowest possible energy range (10 eV to ~ 1 keV). This is the range of energetic neutrals produced by superthermal ionospheric ions when they charge exchange with atoms in the thermosphere. It is also the energy range appropriate to charge exchange of accelerating solar wind thermal ions, and to penetrating interstellar neutral gas atoms. Imaging and velocity analysis of such atoms represents an unprecedented opportunity to remotely sense plasma heating processes, their variations on short time scales, and the interstel-



lar medium (Roelof, 1987; Gruntman, 1997). Neutral atoms with energies greater than ~ 1 keV are the target populations for the IMAGE Medium Energy Neutral Atom imager (MENA), and High Energy Neutral Atom imager (HENA). Imaging of neutral atoms with lower energies presents a different set of opportunities and technical problems, around which the development of LENA has revolved.

The LENA sensor depends for its operation on the conversion of incident neutral atoms into ions that retain the general characteristics of their parent atoms. These are velocity-analyzed by conventional techniques of electrostatic and time-of-flight analyses, then detected and imaged by conventional charged particle techniques. Conventional charge exchange cell techniques are impractical for space flight applications, while the carbon foils used by MENA and HENA cannot be penetrated by such low energy atoms. Thus, the method of choice for conversion is charge exchange upon reflection from a solid surface. Incoming neutrals are converted in part to negative ions that are nearly specularly reflected from the surface, then accelerated and collected by an ion extraction lens that focuses and disperses them in energy. They are passed through a broom magnet that removes electrons, and an electrostatic analyzer that maintains energy dispersion while removing photons, then delivered at high energy to a time-of-flight sensor and 2D imaging system that sorts the particles by polar angle of arrival and energy. The original concept for LENA was described by Herrero and Smith (1986). The optics scheme actually used in LENA was described by Ghielmetti et al. (1994) and Wurz et al. (1995), while an alternative optics concept for LENA was described by Smith et al. (1998).

2. Science Objectives

Development of the LENA imager was motivated by the opportunity such an instrument would provide for remote sensing of plasma heating in the terrestrial ionosphere. Solar wind-driven plasma heating is known to remove a highly variable (in space and time) mass flux of plasma from the ionosphere and to supply it to the magnetosphere and downstream solar wind (Moore and Delcourt, 1995). While ionospheric outflows are known to be highly variable in time (Moore et al., 1999), it has been difficult to study this variability on short time scales and to thereby understand the energy flows that drive the outflows. Most studies have been statistical in nature and have dwelt upon mass flux relationship to indices having variation time scales from a few hours to 11 years. These have been based upon spacecraft orbital precession to sample spatially with a time resolution of several months, if not years (Collin et al., 1998). With remote sensing of ionospheric heating and outflows, we have the opportunity to study ionospheric heating variations at the ultimate time resolution of the imager, as short as two minutes for the spin period of the IMAGE spacecraft.

The nominal $1.25 \times 8 R_E$ orbit of the IMAGE spacecraft will provide a broad range of vantage points for the observation of ionospheric plasma heating, from



Figure 1. Exterior photograph of the LENA sensor, illustrating its main features.

close-ups of the auroral zone at perigee, to global sampling of the entire auroral oval from apogee. In addition, the region of warm heated plasma just outside the plasmopause, in the equatorial plane, will be imaged, and possibly the inner parts of the plasma sheet. LENA provides a $90^\circ \times 8^\circ$ field of view swept by the spacecraft roll to produce an image of $90^\circ \times 360^\circ$ in 12×45 pixels of $8^\circ \times 8^\circ$, through a $\sim 1 \text{ cm}^2$ aperture. It responds in 3 coarse energy bins of $\delta E/E \sim 100\%$ over either of two energy ranges (10–300 eV and 25–750 eV). The mass of the neutrals is determined to support imaging of two ionospheric species (nominally H^+ and O^+) with monitoring of other species at coarse mass resolution of $\delta M/M \sim 0.25$.

In this way LENA will address the following science objectives or questions: (a) How is plasma heating distributed instantaneously within the ionosphere? (b) How and why does auroral plasma heating vary on short time scales ($< 5 \text{ min}$)? (c) How is plasma heating driven by solar activity and solar wind conditions? These science questions lead directly to the measurement objectives of the LENA imager, which are implicit in its name.

3. Instrument Description

3.1. OVERVIEW

Figure 1 is a photograph of the exterior of the LENA sensor, with the cylindrical aperture cover in place. The LENA sensor and control and data handling unit (C&DH) are separated for thermal control reasons, it being desirable to operate the LENA sensor at relatively low temperatures to facilitate high voltage (HV)

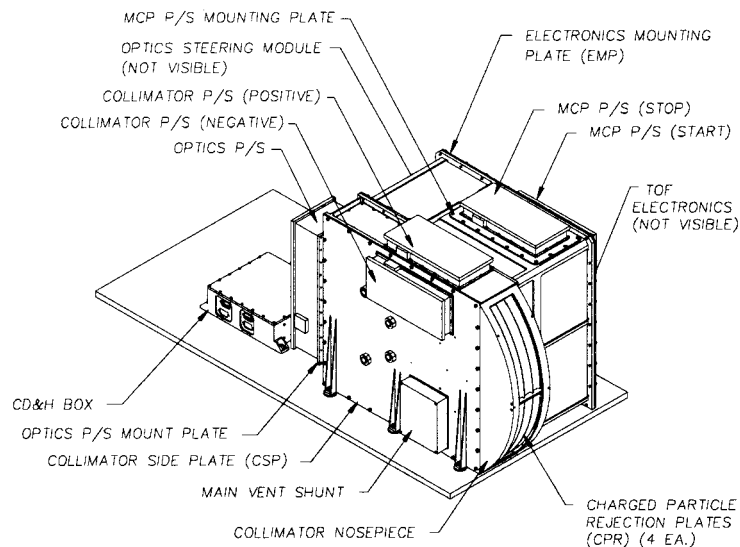


Figure 2. Exterior assembly view of the LENA sensor and its Control and Data Handling System.

operations. The C&DH is the site of greatest energy dissipation in the instrument, so it is thermally coupled to the spacecraft deck plate to prevent it from overheating, while the LENA sensor is thermally isolated and loses energy to space through its entrance aperture structure. The entrance aperture of the instrument has a thermal coating that enhances radiative loss to space.

Figure 2 illustrates the relative placement of the sensor and C&DH on the spacecraft payload deck. The sensor has a number of high voltage power supplies and the time-of-flight electronics unit mounted on it externally, in positions allowing direct feedthroughs to the relevant HV devices or the TOF analyzer, eliminating external HV cabling. These units are highly modular and individually removable from the sensor housing for servicing. The outer housing of the instrument (mostly magnesium) is treated with Dow-9 black, while the electronics units are Alodined. Interior surfaces of the instrument are treated with Dow-9 black if they are magnesium, or with nickel black, chrome black, or gold black (in the most critical areas), for UV suppression.

The sensor is designed with a housing that seals tightly with O-rings as a diffusion barrier against chemical, water vapor, and dust contamination of the sensor interior. As for other instruments using open MCP detectors, LENA's MCPs are sensitive to hydrocarbon contamination and are also strongly hygroscopic. The sealed sensor housing is kept backfilled with gaseous high purity nitrogen. The aperture is the sole vent opening, and is fitted with a purge cover that is removed before flight. The venting conductance of the entrance aperture is augmented by baffled vents for all parts of the interior of the instrument housing.

Figure 3 shows the location and orientation of the LENA sensor relative to the exterior of the IMAGE spacecraft, with field-of-view indicated. The LENA field of

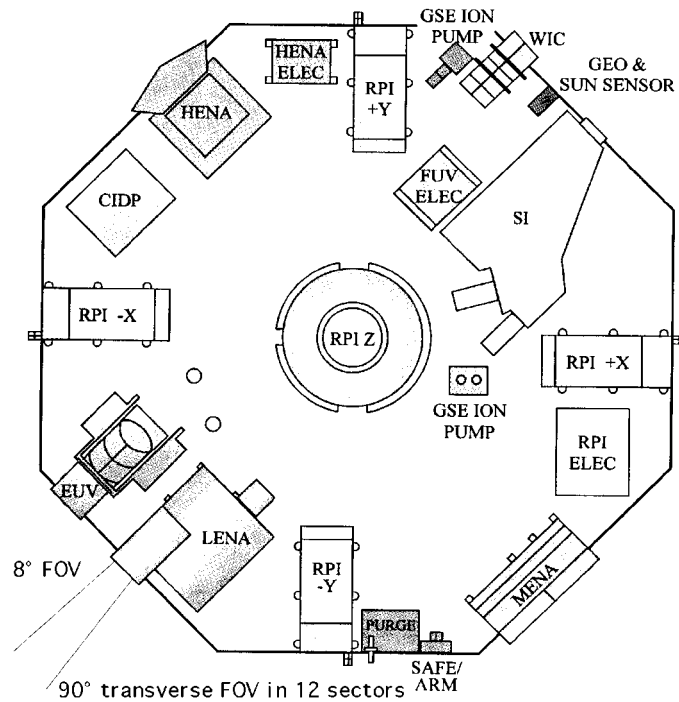


Figure 3. A view of the IMAGE spacecraft, along its spin axis, showing LENA and its pointing and mounting layout. Note that the 90° LENA FOV is centered on the radial direction.

view is a segmented fan coplanar with the spacecraft spin axis and centered on the radially outward looking direction. Each spacecraft spin (120 s, nominal), therefore sweeps out a $90^\circ \times 360^\circ$ swath of the sky, leaving two polar blind spots of 45° polar angle width.

Exterior to the conversion surface, LENA is a pinhole camera with a $\sim 1 \text{ cm}^2$ 'pinhole'. Figure 4 illustrates in three dimensions the main components of LENA and the optics path through it. A two dimensional optics cross section is given in Figure 8. An optically polished near-conical conversion surface (consisting of 4 facets of 22.5° width each) intercepts incoming neutrals passed by the collimator/charged particle rejector at an incidence angle of 75° from normal. As the atoms are converted, they are reflected approximately specularly, with $\langle E_t \rangle \sim 0.60\text{--}0.80 \cdot E_i$, where these are transmitted and incident energies and the brackets indicate an average. The surface, maintained at a nominal high voltage of -20 kV , converts incident atoms to negatively charged ions of corresponding species (or in some cases sputters surface adsorbates as negatively charged ions, as described in Appendix A).

The emitted negative ions are accelerated, focussed and dispersed in energy by an ion extraction lens. The lens can be trimmed to an energy range between $10\text{--}300 \text{ eV}$, up to $25\text{--}750 \text{ eV}$, using a commandable photodiode in the lens re-

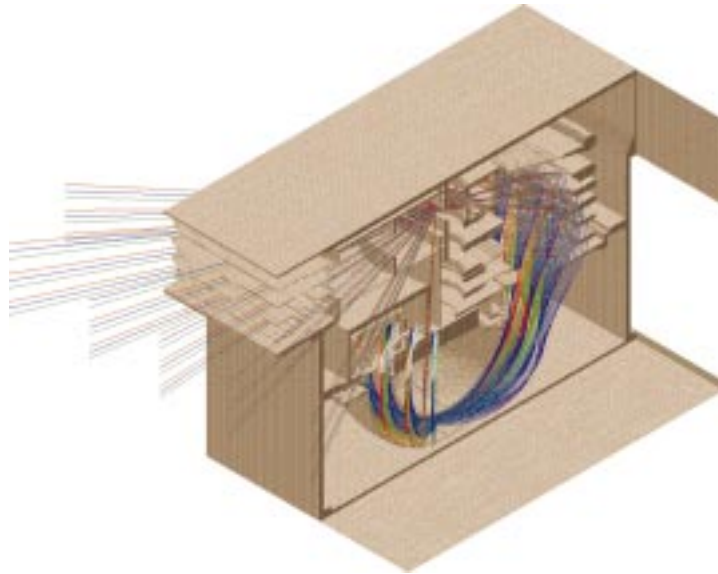


Figure 4. Section view of the LENA sensor showing the optics path through the collimator to the conversion surface, the ion extraction lens, electrostatic analyzer, and ITOF analyzer. The plotted rays illustrate the full range of polar angles, while the colors indicate low, medium, and high energy particle behavior. Reference is made to Figure 8 for a 2D section of the instrument, with component labeling.

sistor chain. A broom magnet removes photoelectrons or other electrons emitted by the surface, if they fall within the LENA energy acceptance. Negative ions are then passed to a spherical electrostatic analyzer that maintains the radial energy dispersion of the ions as it removes residual UV photons and passes the negative ions to the imaging time-of-flight (ITOF) system for mass, energy, and polar angle analysis. They arrive at the ITOF system with energy corresponding to the optics high voltage, nominally 20 keV.

The ITOF system consists of carbon foil apertures, a harp mirror system that reflects secondary electrons emitted from the back sides of the foils, and four sets of start and stop detectors (one for each conversion surface facet). The detectors are chevron stacks of microchannel plates with $L/D = 60$. The start stacks are rectangular, while the stop stacks are trapezoidal corresponding to projections of the conversion surface facets. Start event charge clouds fall directly upon a 2D wedge and strip anode (Walton et al., 1978) with four preamplifiers, the ratio of whose pulses define radial and polar angle coordinates for the events. The preamplifiers are located within the TOF detection unit, and pulses are passed to the Position Sensing System in the C&DH box. Start and stop events generate fast pulses regardless of their point of impact on the detector system. These are passed directly from the fast pulse anodes to the TOF electronics unit.

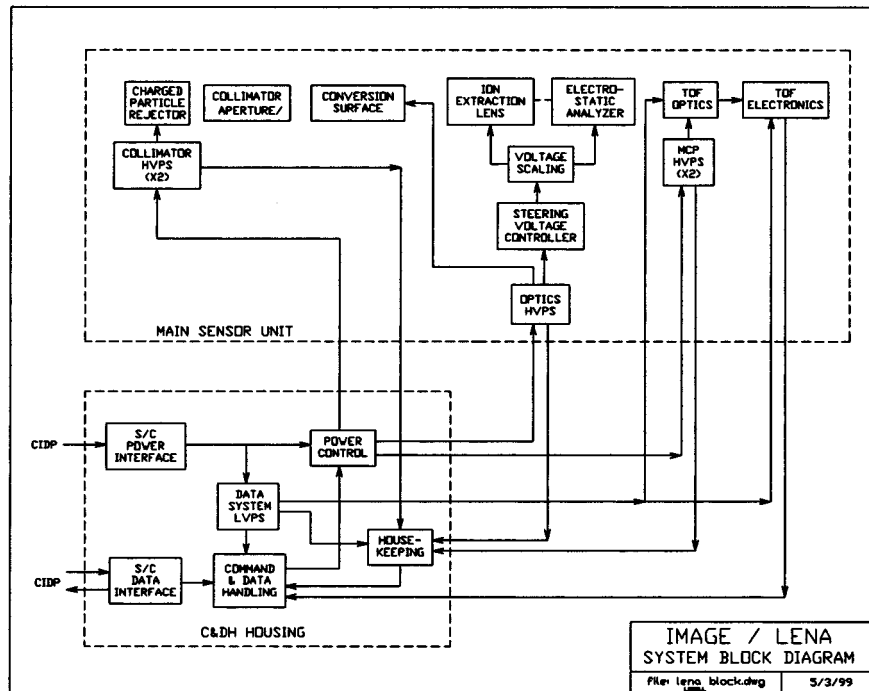


Figure 5. Functional block diagram, showing the relationships among the principal components.

LENA data products include a combination of (a) image data for each of two standard masses (H and O) and 3 standard energies (15, 60, 240 eV, or 30, 120, 480 eV), giving a total of 3240 data points ($12P \times 45Az \times 3E \times 2M$), (b) mass spectral data for a selected region of interest or the entire image, and (c) direct events including full energy, polar angle, mass, and energy information. LENA is simplified by its lack of any swept potentials (except possibly the steering controller that varies the energy range; intended to be changed occasionally).

LENA is controlled by a field-programmable gate array (FPGA) that processes events from the position sensing system and the TOF electronics and by an 8051 microcontroller that sets up data products for transmission to the spacecraft central instrument data processor (CIDP). The microcontroller also queues commands, executes them at the next suitable opportunity, and transmits data to the CIDP. Additional details are provided in Appendix B. The overall organization of the instrument is summarized in Figure 5 at the subsystem block diagram level.

3.2. SPECIFICATIONS

The fundamental design goal for LENA was to achieve conversion of low energy neutral atoms to negatively charged ions that can be analyzed and detected using conventional methods. LENA has also been designed to provide coarse 2D

TABLE I
LENA specifications

Parameter	Value
Energy range (incident neutral atom)	15–1250 eV
Energy resolution	$E/\delta E = 1$ at FWHM
Mass range	1–20 amu (H^+ and O^+)
Mass resolution	$M/\delta M = 4$ at FWHM
Angular coverage	sampling: $8^\circ \times 8^\circ \times 12$ sectors per spin: $360^\circ \times 90^\circ$ in 45×12 samples
Angular resolution/response	$8^\circ \times 8^\circ = 0.02$ steradians
Total field of view	2.8π sr
Pixels per Image	$3.2k = 3 \text{ Energy} \times 45 \text{ Az} \times 12 \text{ Polar} \times 2 \text{ mass}$
Pixel physical aperture	$1.0 \text{ cm}^2 (A_{\text{eff}} \leq 1 \times 10^{-3} \text{ cm}^{-2})$
Pixel solid angle	$0.02 \text{ sr per pixel} \times 12 \text{ pixels}$
Time resolution 1D Polar \times Energy	2.7 s
Time resolution 2D (Az \times Polar) \times Energy	120 s
Time resolution 3D (Az \times Polar \times Energy)	1 spin period (120 s)
Dynamic range	10^4
Resources:	
Mass	20.75 kg
Power	13.1 W orbit averaged
Telemetry	0.5 kbps

imaging (using spacecraft spin) of the angular distribution of the flux of such low energy neutral atoms. Finally, LENA has also been designed to implement a coarse separation of the converted neutrals by energy and by mass.

Time resolution is the principal objective of the LENA effort to remotely sense plasma heating at the lowest energy levels. In the past, it has been necessary to exploit the slow evolution of a spacecraft orbit to obtain an adequate spatial distribution of *in situ* phenomena such as auroral plasma heating. This means that the temporal resolution with which the spatial distribution can be studied is comparable to the precession period of the spacecraft, usually several months to a few years. With remote sensing of the same phenomena, the spatial distribution can be discerned with adequate spatial resolution once per spin exposure, or a few minutes. This represents the fundamental quantum leap that remote sensing offers. In particular, a basic goal of the IMAGE mission is to resolve temporal variations on substorm time scales, i.e., shorter than 1 hour, down to several minutes.

Table I provides a summary of the technical specifications for LENA which details the resolution and sensitivity of the instrument.

3.3. COLLIMATOR-CHARGED PARTICLE REJECTOR

The path of particles or photons incident upon the LENA aperture begins with passage through a combined collimator and charged particle rejector system (CPR). The vanes of this system are positioned to eliminate trajectories that would in any case be unacceptable to the LENA optics system; that is, trajectories which lie outside the angular response and effective aperture of the instrument. This collimator approach is intended to minimize the number of extraneous particles and photons entering the instrument apertures, and particularly to eliminate such particles or photons which would otherwise be incident upon interior surfaces other than the conversion surface. In this way, the susceptibility of the instrument to extraneous particles and photons is minimized. Collimation of 8° width in spacecraft azimuth is provided by means of radiating vanes.

As discussed below, the CPR vanes are a potential source of fast neutral atoms, formed when incident charged particles are converted to or otherwise produce secondary fast atoms upon striking the vane surfaces. To assure that such atoms cannot reach the conversion surface (described below), the vanes are fitted at their inner edges with 'fences' that eliminate straight line paths from the vane surfaces, through the entrance aperture S1, to the conversion surface.

The four vanes are electrically insulated from chassis for high voltage operation, and are alternately biased at positive and negative potentials that are separately controlled. The effect of the resultant electric field on entering charged particles is illustrated in Figure 6. The plate geometry is designed for rejection of particles at up to 100 keV incident energy, making the instrument resistant to the entry of magnetospheric ions and electrons at energies up to the ring current range, above which fluxes fall rapidly. Together with the entrance aperture and slit S1, the collimator defines the field-of-view over which LENA can accept particles, as specified in Table I.

3.4. CONVERSION SURFACE SYSTEM

Fast neutral atoms in the energy range below 1 keV are severely scattered and degraded in energy by even the thinnest of foils, and are ineffective in producing secondary electrons when interacting with surfaces. Fast atoms routinely escape from laboratory plasmas owing to charge exchange with residual gas. These can be converted to ions for analysis, analogous to the LENA measurement objectives. A partially ionized charge exchange cell is often used for this in the laboratory (Fasola, 1977). This approach requires differential pumping in the laboratory to achieve cell pressure around 10^{-2} Torr, and is thus highly problematic for a space instrument. Gas released from the charge exchange cell to space would create an enhanced charge exchange medium over some length scale around the spacecraft, potentially creating local fast neutrals from the exterior ion plasma, contaminating the desired signal.

Collimator/Charged Particle Rejector

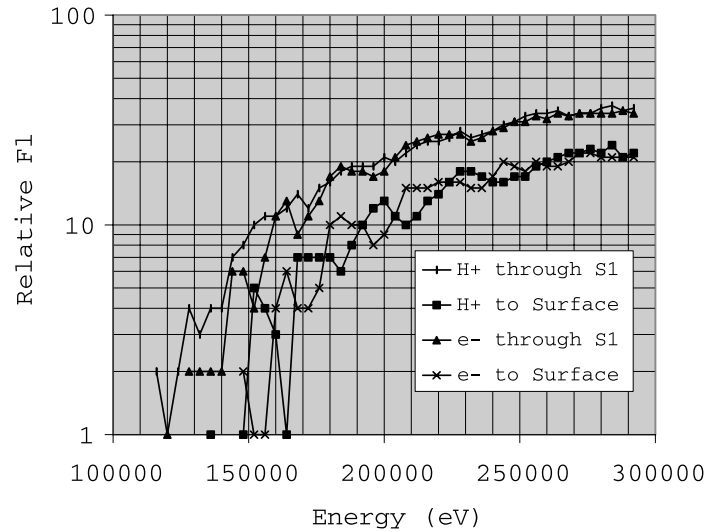


Figure 6. Results of a simulation of the LENA charged particle rejector, showing cutoff for particles with energy less than about 100 keV.

To confine the conversion region and improve the conversion probability, it is useful for the incoming atoms to be incident upon a solid highly polished surface. A significant fraction of the incident atoms is near-specularly reflected from a surface polished to sufficient smoothness. As nearly all surfaces in vacuum are coated with water molecules and other adsorbates, there is a significant probability of conversion to a negative ion (for species such as H and O, with stable negative ion states). More detailed discussion of surface conversion, including the angular distribution of the emitted negative ions, is provided in Appendix A.

The central element in LENA is thus a conical conversion surface (CS) composed of four flat facets, each a trapezoid of optically polished tungsten (W). The four surfaces are illuminated with neutral atom flux through the collimator/charged particle rejector, and main aperture. The entire structure that supports the CS, shown in Figure 7, is floated at a high negative potential in the range from 15–20 kV. The conversion product negative ions (and any secondary electrons produced on the surface) are accelerated away from the CS support structure and collected by the LENA ion optics system.

3.5. ION OPTICS SYSTEM

The LENA ion optics system consists of an ion extraction lens (IXL) and an electrostatic analyzer (ESA). Together these subsystems collect negative charged particles from the CS, separate out any secondary electrons by means of a broom magnet, and image them across slit S3 according to their arrival angle (polar angle

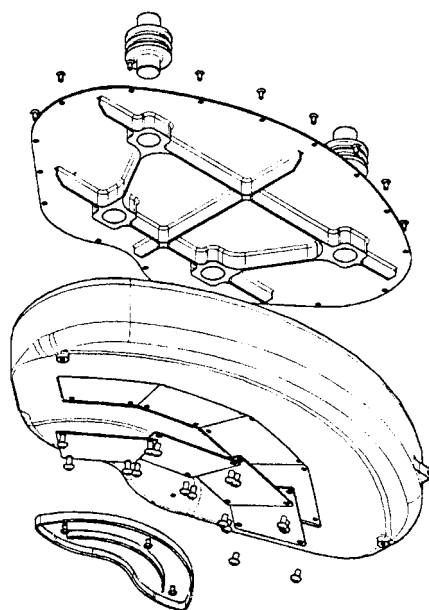


Figure 7. Isometric view of the conversion surface mounting structure.

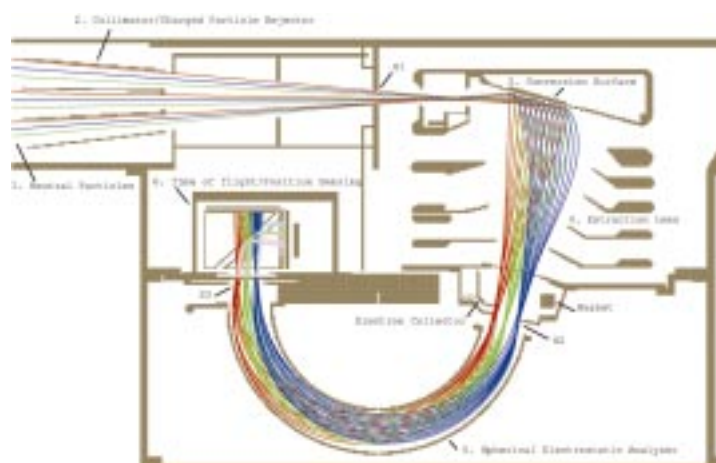


Figure 8. End-to-end simulation of the ion optics of LENA, also showing the TOF optics in a 2D section through the symmetry axis of the instrument.

relative to the s/c spin axis), and their energy (radius across S2, more energetic ions at larger radius, and vice versa at S3 after inversion through the ESA). The imaged ions are delivered to the time-of-flight (TOF) analyzer for detection, binning by polar angle and energy, and analysis by mass. The system is depicted with end-to-end simulated raytracing in Figure 8. Optics simulations were performed using SIMION (Dahl, 1995).

The IXL consists of a stack of electrodes that are biased at potentials intermediate between that of the CS and ground. The electrodes define an immersion lens that collects negative particles from the CS, and images them upon slit S2, according to their arrival angle and their energy. The IXL plates are biased relative to the optics HV applied to the CS using a high impedance resistor chain that is integral with the lens structure. One of the electrodes is biased with a variable resistor that is commanded by means of an opto-coupler, the steering controller (SC). The most energetic ions are mapped to the largest radius at S2; and a 1-1 mapping is made between the energy of emission at CS and S2 passage, apart from transverse components of the emission velocity.

The ESA consists of a pair of truncated hemispherical plates designed to map the arrival angle and energy of the particles from S2 to S3, where they are passed on to the TOF analyzer. The energy distribution is reversed so that highest energies are found at lowest radius at S3. The ESA is biased using the same resistor chain that biases the IXL, deriving its potential from the optics HV supply.

EUV-induced electron contamination of the TOF analyzer is a serious concern for LENA. To stop EUV penetration, the entire interior of LENA is blackened with either nickel black, chrome black (on Aluminum surfaces) or Dow-9 (on Magnesium surfaces; including the main LENA housing). Moreover, the ESA plates are blackened with Gold black (outer) and chrome black (inner) to further suppress EUV transmission to the TOF analyzer, which is entered through S3, at the output of the ESA. The optics design requires at least three bounces for a UV photon to reach the entrance to the detection system, starting from the conversion surface.

3.6. IMAGING TOF SYSTEM

The imaging TOF subsystem is a self-contained module containing $\sim 2 \mu\text{g cm}^{-2}$ carbon foils at the entrance aperture S3, an electrostatic mirror system, four start detectors and four stop detectors corresponding to the four CS facets, a wedge-and-strip start anode, a preamp board with four Amptek A111a preamplifiers for the wedge and strip position sensing signals, and a stop anode.

Negative ions collected and accelerated by the IXL are incident upon the carbon foils suspended upon grids at S3 at the entrance to the TOF analyzer. Each ion incident upon the foil creates one or more secondary electrons of typically a few eV energy, emitted from the rear of the foil as the ion passes. Within the foil, most of the ions charge exchange to neutrals or positive ions, and suffer some degree of energy loss and angular scattering, but continue generally along their trajectories toward the stop MCP detectors, arriving with a time delay appropriate to their mass/charge. The 20 kV acceleration potential was chosen for energy loss and scattering compatible with adequate mass resolution and position sensing.

The electrons produced at the start foil are accelerated across a gap through which they enter the electrostatic mirror. The mirror is based on a harp design, in which wires are wound on a frame to produce the equipotential grids. As a result,

the electrons are reflected sideways out of the ion flight path and are collected at the start MCP detector, after a delay that is negligible in comparison with the ion time of flight from start foil to stop MCP. Other surface potentials in the vicinity of the start foils are designed so as to insure that the electrons emitted by the foil are forcefully directed toward a point on the start MCPs that corresponds closely to their point of emission from the foils. In this way, the energy and angular distribution of the ions passing through the foils are imaged upon the start MCPs. Sample computed electron trajectories are also illustrated in Figure 8.

The stop MCP stacks are trapezoidal, corresponding roughly to the shape of the CS facets, while the start MCP stacks are rectangular and stacked together off to the side of the ion flight path. The MCP high voltage supplies are commandable over a range up to 1500 V per plate, also allowing for ample gain margin during prolonged operation on orbit. The total number of MCPs is 2 per stack \times 2 sets of stacks \times 4 polar angle facets, or 16 per LENA sensor. The plates have pores of 25 μm diameter, with channel $L/D = 60$, for a thickness of 1.5 mm. The chevron stacks obtain a pulse height distribution with $\text{FWHM} \leq 50\%$. Plate resistances are in the range of 100 $\text{M}\Omega$ per plate. LENA MCPs are handled under clean room conditions and LENA is constructed of materials whose compatibility with long MCP life has been demonstrated by means of lifetime testing. They have been burned in as stacks to $\geq 10^{10}$ counts cm^{-2} .

The wedge-and-strip start anode also includes a capacitively-coupled non-imaging anode used to generate the fast TOF pulse. This and the stop anode fast TOF pulse are fed directly to the TOF electronics through shielded coaxial cables between boxes. The wedge-and-strip charge pulses are delivered immediately to a pre-amplifier board inside the TOF unit. Four A111a charge amplifiers produce relatively slow pulses that are fed to the pulse sensing system (PSS), located on the Command and Data Handling unit logic board, where the pulse amplitudes are sampled and coordinate ratios are computed.

3.6.1. TOF and PSS electronics logic

All fast TOF pulses (start and stop) are counted without regard for the presence of a correlated pulse in another detector. These count rates are termed ‘singles’ rates to distinguish them from the more restricted set of correlated pulses resulting in time-of-flight measurements. In the ideal case the ion passing through the start foil creates one or more secondary electrons. These in turn are all collected and create a corresponding start pulse in the MCP. The ion (or neutral) then proceeds from the foil to the stop MCP and there creates a stop pulse. In fact, none of these events has a unity probability and the expected efficiency of the entire TOF event chain is ~ 0.2 . In addition, there are random start and stop signals due to penetrating radiation (in space) and to noise in the individual MCPs (spontaneous emission of secondary electrons) giving rise to random coincidences. The possible cases may be summarized as follows:

Start/valid stop: in this case a ‘coincidence’ pulse is generated and, at the conclusion of the process, a valid TOF value is also generated. In addition, the four PSS pulses are captured and used to form the 2D coordinates of the valid coincidence event.

Start/no stop: In this case the TOF circuit ‘times-out’ at a predetermined maximum time (300 ns). The resulting TAC signal is not analyzed by the ADC because it contains no information and would only slow up processing. Neither are the PSS pulses processed, unless the instrument is operating in the ‘starts-only’ mode. A ‘time-out’ signal is generated for each such event.

Start/second start/stop: after the first start pulse the TOF circuit ignores any further start pulses that occur before either a stop pulse or a ‘time out’. Subsequent start pulses which occur during the 300 ns TOF window (actually 1 ms, including overhead) are not processed, and this time therefore serves as a (non-paralyzable) dead time for the circuit. The chance probability of a valid second start within the time-out window is small unless the count rate is extremely high, which would not ordinarily be permitted (see below).

Stop/No Start: the logic does not respond to a stop pulse unless a valid start pulse has occurred within the previous period. By definition a start event is required to fire the logic.

Start/Stop in Random Coincidence: nothing can be done about this possibility and a random TOF value is recorded. However, note that truly random coincidences are scattered uniformly across the TOF spectrum and this background can, in principle, be measured and subtracted. The expected rate for random coincidences is: $R_{12} = R_1 R_2 t$ where R_1 and R_2 are the start and stop detector random rates, and t is the TOF dead time of 300 ns. Taking $R_1 \sim R_2 \sim 100 \text{ s}^{-1}$ for all seven start and stop MCPs (which would correspond to relatively high background levels) gives:

$$R = (10^2)(10^2)(3 \times 10^{-7}) = 3 \times 10^{-3} \text{ s}^{-1} . \quad (1)$$

Thus the random rate should be relatively low, if the MCPs can be kept to low background rates. This also means that in the presence of a high flux of ions the random coincidence rate increases because it is proportional to either of the singles rates. LENA radiation shielding consists of a thick outer housing ($\geq 4.6 \text{ mm}$), as well as an internal housing for the ITOF unit. The anticipated radiation noise rate on the MCPs in the worst part of the radiation belts is a few Hz, which would produce a negligible spurious coincidence rate.

At high event rates, the LENA electronics exhibits non-paralyzable dead time effects far before the MCP detectors reach paralyzing rates. The relevant electronic dead times associated with various LENA signals are given in Table II.

TABLE II
LENA Live Times and Dead Times

Signal	Dead time
START singles (no coincidence)	1.0 ms
START singles (coincidence)	1.6 ms
Coincidence events	13 ms
STOP singles	1.0 ms
TOF, MQ PSS data	100 ms
TOF Direct Event data	100 ms
Sample period (live fraction)	2700 ms
Sample period (dead fraction)	0 ms

Note: All values are preliminary.

4. Operations

4.1. LENA RESPONSE

The response of LENA to an incident neutral atom is governed by the dimensions of the collimator, the entrance aperture slit, the conversion surface, the ion optics, the ITOF optics, and finally the response of the detectors. The detector can be configured to measure either the total incident neutral atom flux or to determine the composition of the incident neutral atoms through the time-of-flight technique. The response is fully described by the product of the effective aperture area (δA), the pixel solid angle ($\delta\Omega$), and the energy range (δE) for each accumulation. In practice, these quantities may be functions of the incident particle species or energy, and of internal potentials applied to the optics elements or to the MCP detectors. Below we discuss each these factors in separate subsections, as it relates to the overall response. Finally we will discuss potential sources of noise, against which the signal will be recorded.

The instrument was calibrated at the University of Denver atomic beam facility and at the GSFC ion beam facility. In the latter case, neutral atoms were created by means of fast-ion charge transfer collisions with the background gases inside the vacuum chamber. While the GSFC neutral atom beam was not well characterized with respect to energy, it did provide the ability make an end-to-end test of the instrument and to map out the relative response of the instrument with respect to incoming angle. At the Denver beam facility the LENA instrument was mounted on a two-axis rotation table allowing for angular response measurements. The instrument was placed in a vacuum chamber such that it intercepted the neutral atom beam.

The experimental arrangement and procedures for generating atomic oxygen and hydrogen beams at the Denver facility have been described in detail previously

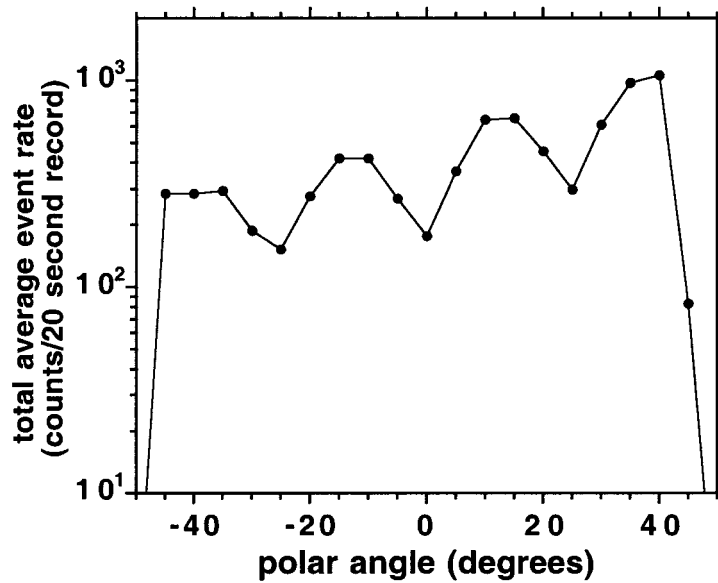


Figure 9. Total counting rate as a function of neutral atom beam angle. The separation between the facets are due to internal stops within the ion optics.

by Stephen et al. (1996). Briefly, O^- and H^- ions are formed in a conventional low pressure (~ 250 Torr) arc discharge source. The ions are subsequently extracted and focused into a region where the well-collimated negative ion beam orthogonally intersects an Ar-ion laser cavity. The intracavity laser radiation photodetaches a portion of the incident beam (typically $\sim 1\%$) while the remaining ions and electrons are extracted from the beam, leaving only the desired neutral beam continuing onward toward the target. The intensities of the atomic beams formed in this manner are measured via an optical chopping technique. The operating wavelength of the Ar-ion laser ranges from 488 to 514 nm ensuring both O and H atomic beams are formed entirely in the ground state, since the electron affinities of O and H are 1.46 eV and 0.75 eV respectively and their first excited states lie 1.97 eV and 10.2 eV above the ground state, respectively. Additional details are given in Appendix A.

4.1.1. Angular Response

LENA is designed to have a 90° polar by 8° azimuthal acceptance angle about the entrance aperture. This angle is defined geometrically by the collimator and by the dimensions of the conversion surface. The polar angle is subdivided into twelve 7.5° polar bins, while binning of azimuthal angle and imaging of the neutral atoms is achieved through rotation of the spacecraft. Conversion of neutral atoms takes place on four distinct tungsten surfaces equally spaced across the polar angle dimension. Each surface is associated with distinct microchannel plate assemblies for both the start and stop sections of the TOF system as well as distinct carbon foils.

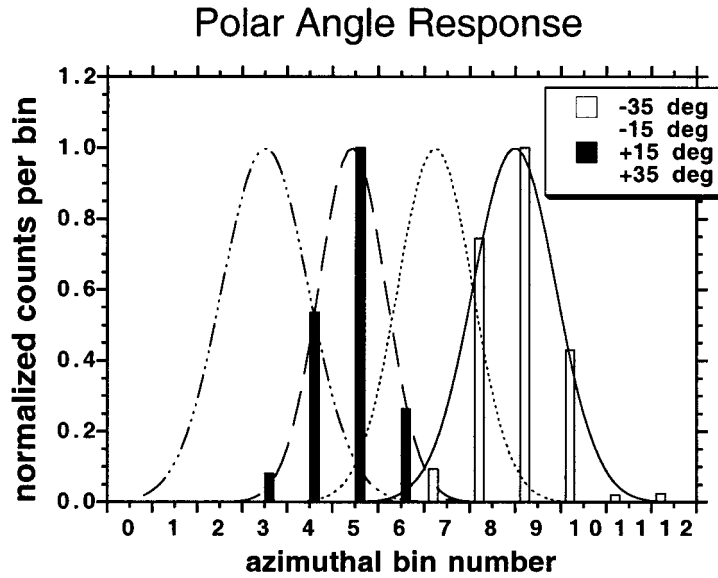


Figure 10. Response function in polar angle, for several fixed incoming beam direction. The distribution across angular bins are fitted to Gaussian functions with an average FWHM of 2.5 bins for each of the beam angles.

As illustrated in Figure 9, within any one of these four angular sections the relative efficiency for detection of neutral atoms was constant but among the sections the efficiency varied by as much as a factor of three.

As described previously, the polar angle of a detected neutral atom is measured with the position sensing anode on the ITOF start detector. The angular resolution is limited by angular scattering of the atoms on the conversion surface, optical aberrations in the ion extraction lens, scattering of the detected secondary electrons from the carbon foil, and measurement error on the position sensitive detector. These aberrations lead to a dispersion in the angular response as illustrated in Figure 10.

4.1.2. Energy Response

LENA was designed to operate over neutral atom energy ranges of 10 to 300 eV and 25 eV to 750 eV depending on the potential placed on the steering electrode. Within these ranges, these measured energies correspond to those of the scattered negative ion from the conversion surface. Particles incident on the surface lose energy over a broad distribution which is peaked at about 60% of the incident energy for oxygen and 80% for hydrogen. In addition, low energy negative ions, sputtered from the surface by the incident neutral particle, contribute to the signal. The ion extraction lens on LENA is designed to focus and disperse the scattered ions according to energy across the carbon foil detector plane on the TOF analyzer (Slit S3). The location of the incident ions on the carbon foil is determined by imaging the secondary electrons from the carbon foil onto a position sensitive

detector. In this way, both a measurement of the energy and angle (orthogonal to the energy axis on the PSD) of the ions are simultaneously determined.

Owing to schedule pressure on the IMAGE mission and development problems with LENA, it was not possible to characterize the LENA energy response adequately. Specifically, it was not possible to determine the true energy boundaries of the three energy bins. Unless additional calibration time becomes available, it will be necessary to base the energy passbands for the three bins upon simulation results. The nominal energy bins (at 20 kV optics potential) are centered at ~ 50 , 150 and 250 eV (ion energy) at the lowest steering potential. At the highest steering potential, the bins are shifted to ~ 300 , 500 and 700 eV, respectively. These energy ranges scale approximately with the optics potential in use at any given time and the numbers above correspond to the nominal optics potential of -20 kV.

4.1.3. *Time-of-Flight Response*

LENA includes a carbon foil TOF analyzer designed to separate converted hydrogen from converted heavy ions. An example of the TOF spectrum is shown in Figure 11. The spectrum shows clear separation of the well-peaked H atom signal and the O atom signal which is more broadly distributed owing to straggling in the foils. This spectrum was taken with an incident oxygen atom beam but the spectrum includes H atom signal due to the sputtering of these atoms from the tungsten surface. Since the sputtered atoms come off the surface with low energy, relative to the energy of the scattered atoms, it is possible to remove most of the sputtered atoms from the detector by using the steering electrode. This is shown in Figure 11 where the ratio of hydrogen to oxygen changes from 1.78 in the upper panel to 0.07 in the lower panel. When the sputtered ions are not removed, compositional information is lost but the sensitivity of the instrument is improved.

4.1.4. *Effective Area*

We define the effective area of the instrument to be the product of the aperture area and the probability that a neutral atom entering through the aperture and hitting the conversion surface (and therefore within the field of view of the instrument) will be detected. The effective area is strongly affected by the conversion efficiency on the tungsten surface, the transmission of the extraction and imaging optics, and the efficiency of the carbon foil TOF analyzer. The efficiencies of atom conversion and TOF detection are also dependent on the converted ion species. These efficiencies are in turn affected by commandable settings of the ion extraction lens voltage, the microchannel plate bias voltages on the TOF start and stop detectors, the channel plate gain, the detector threshold level settings, and the noise floor which limits the extent to which the threshold level settings can be lowered. Using the University of Denver neutral atom beam facility we made measurements of the absolute efficiency of LENA for H and O atoms. These measurements were initially made at suboptimal MCP biases, owing to problems with ion feedback in the MCP stacks. These problems were later corrected and the efficiency of the

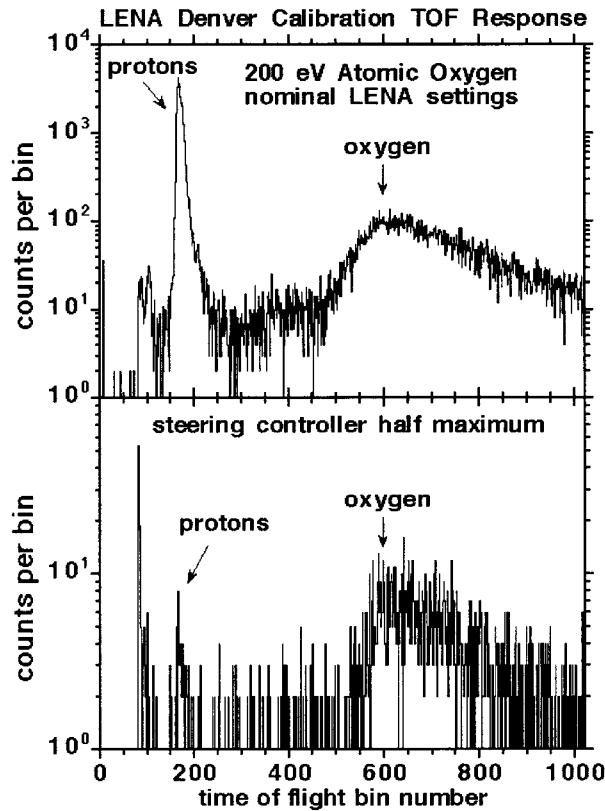


Figure 11. Upper panel: TOF response to oxygen including sputtered H atoms. Lower panel: TOF response to oxygen with steering voltage set to remove sputtered atoms. The integration time in the upper panel is 7.1 times larger than in the lower panel, and very little of the converted oxygen is removed from the beam when the steering controller is exercised.

MCPs when operating at DU was determined to be 0.25 of their full efficiency when optimally operated. Figure 12 shows the estimated efficiency based on best knowledge including both DU and GSFC testing results.

4.1.5. Time Dependence

Work at the University of Denver indicates that conversion on the tungsten surface is taking place on adsorbed species, most likely water, rather than the tungsten itself. During tests of the surfaces, conversion signal disappeared after heating the surface to 800 K, but reappeared after the surface cooled and adsorbates reformed on the surface, within about 30 min (at 10^{-8} Torr). We also found that the energy distribution of the converted ions from a 300 eV (equivalent energy) neutral atom beam does not exhibit the elastic scattering peak that is evident when negative ions are scattered from the surface with no charge exchange taking place. In previous experiments by Taglauer (1985), the elastic scattering peak has been attributed to

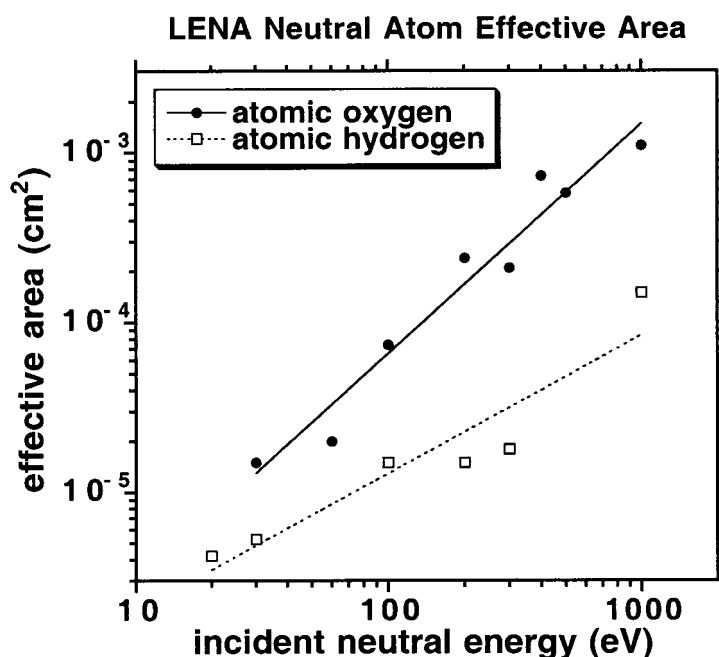


Figure 12. Measured effective area as a function of neutral beam energy. Since the optics high voltage supply may not be exercised at the highest designed setting of 20 keV initially, we include Figure 13 which shows the dependence of efficiency on the optics voltage. The drop in efficiency for lower optics voltage settings is primarily due to increased ion scattering and low secondary electron yields in the carbon foils as the energy of the ions are reduced.

collisions with the surface, while the broad inelastic peak was assigned to collisions with adsorbed molecules.

Over time on orbit much of the water will evaporate but at least a monolayer of water or other chemical adsorbates remains on the conversion surface at laboratory pressures. The surface may be further modified by the application of solar UV radiation. Experiments were performed in which the surface was illuminated with an Ophos UV lamp that emulates the solar $L\alpha$ line. It was found that no change was produced in the surface conversion efficiency for effective exposure durations of order of ten days, again at operating pressures of 3×10^{-8} Torr. Ultimately, the best knowledge of conversion surface stability in the long term will be obtained from experience on orbit, and possible intercalibration with the MENA instrument.

4.1.6. Noise

Potential sources of noise include electronic noise, signal due to high energy ions that make it through the collimator, photoelectrons, and photo-desorbed negative ions. The collimator is designed to reject incoming ions through the application of a strong electric field between parallel plates, as shown previously. Ions above the

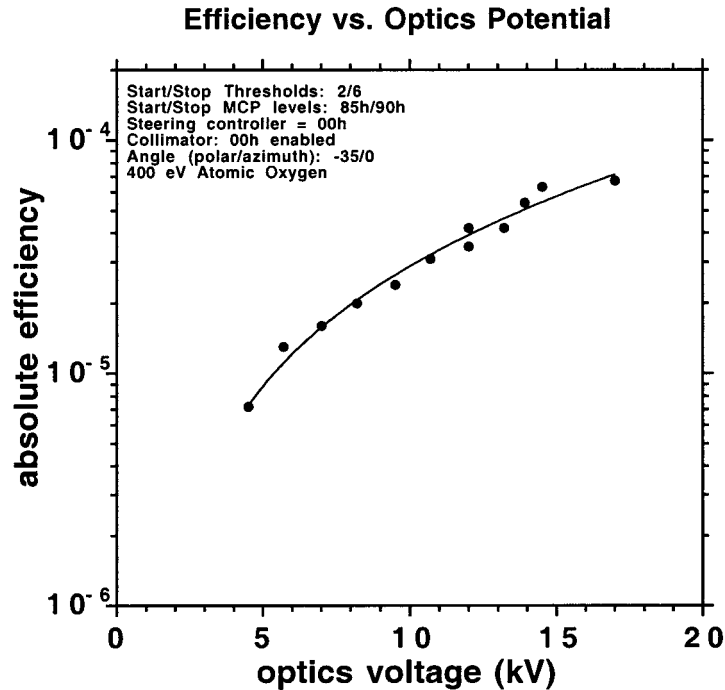


Figure 13. LENA efficiency (dimensionless) variation with optics potential.

rejection threshold will impact the conversion surface and sputter ions that will be detected but their flux is expected to be negligible on the IMAGE spacecraft orbit.

The detector on LENA is well protected from light and photoelectrons by the extended multiple bounce path from the entrance aperture to the detector and through the use of photon and electron absorbing materials in the spherical analyzer section. Photoelectrons are further suppressed by a small magnet located at the entrance of the spherical analyzer section. More problematic for LENA is the systematic noise due to photo-desorption of negative ions from molecules that are absorbed on the conversion surface. These negative ions, chiefly O^- , OH^- and H^- derived from water adsorbed to the conversion surface, are distinguishable from the converted fast neutrals by their translational energy after leaving the surface. We conducted laboratory measurements of the response of LENA to far UV light near $L\alpha$. These measurements provide an upper bound to the expected photo-desorption noise limit. For the expected average on-orbit geocorona $L\alpha$ intensity of 10 kR we anticipate not more than 20 counts s^{-1} pixel $^{-1}$. This is an upper bound because the measured signal includes contributions from two alternative processes which we should not observe on orbit owing to the superior vacuum ($<10^{-8}$ Torr in space vs. 10^{-6} Torr chamber pressure) that will be present there. These are (1) dissociative attachment of neutral molecules above the conversion surface by photoelectrons generated on the conversion surface and (2) negative ion sputtering from acceler-

ated positive ions that are generated by ionization of background gas above the surface.

4.2. COMMANDING OPTIONS

The overriding philosophy of the LENA instrument design was to keep the instrument as simple as possible and sweep free by imaging all relevant parameters. Since there is little that can be modulated, the number of operating modes is small. LENA will, in general, be operated at fixed settings during the lifetime of the mission following the initial ramp-up to nominal voltage levels.

The collimator voltage does not affect the instrument response to neutrals, as expected, so that the intent is to run the collimator at the highest practical voltage level to eliminate any background due to ions or electrons. Although the collimator has not yet been beam tested to evaluate the degree of effectiveness in eliminating ions, this being an anticipated post-launch effort, simulations suggest that the collimator eliminates all ions with energies a factor of ten greater than their voltage setting. Consequently even a modest collimator setting of ± 3.28 kV, which was routinely run during calibration, will shield LENA from ions with energies below 32.8 keV.

LENA azimuthal information is obtained naturally through the rotation of the IMAGE spacecraft at 0.5 revolutions min^{-1} . Polar information is obtained using the position sensing start anode in the time-of-flight section of the instrument and is always available although the resolution increases with the post-acceleration, that is the optics supply level. Likewise, mass differentiation is effected by the time-of-flight unit as well, based on the amount of time required by fixed energy ions to traverse a fixed distance. Once again, however, primarily because of scattering and energy loss in the $2.0 \mu\text{g cm}^{-2}$ carbon foil, time-of-flight, that is mass, resolution increases with the post-acceleration or optics supply level.

4.2.1. Operation and Commanding

The operating state of LENA is set by implemented commands. Of these, the most important are as follows, in roughly the order in which they are exercised to bring LENA up to full operation:

Accumulation period and spin synchronization: LENA can either free run with a specified accumulation period, or can be synchronized with the IMAGE spin clock. The former capability is necessary at times when the IMAGE spin clock signal is not available for any reason.

TOF test pulser: this can be actuated at any time, and used to verify the operation of the fast pulse amplification and time-of-flight analysis by the TOF electronics.

MCP HVPSs: normally, the start and stop MCP supplies are unsafed, enabled, and commanded to their operating levels before any of the other supplies. The MCPs provide very sensitive detection of any charged particles present inside the sensor and therefore provide early warning of any incipient corona or dis-

charge condition. While this has rarely been a problem for LENA, this procedure is observed as a precaution.

Collimator HVPSs: the collimator supplies (positive and negative) are unsafed, enabled, and commanded to their operating levels next. Capable of ± 8.8 kV, nominal operation is at 8.0 kV. However, considerable rejection of energetic ions and electrons is provided at lower levels.

Optics HVPS: the optics supply provides the potential required to bring LENA into full operation by accelerating negative ions produced by the CS into the optics and the TOF analyzer. When unsafed and enabled, it assumes an output voltage of approximately 2 kV. The instrument begins to operate usefully at approximately 10 kV, and gradually improves in effective area and angular resolution as the potential is raised to 20 kV.

Optics Steering Controller: the variable IXL electrode is controlled by command of its opto-coupler, to slide the energy range up or down as desired.

TOF Analysis: though LENA is intended to perform TOF analysis on all image data, a ‘starts-only’ mode also exists, in which all start events are imaged, regardless of whether or not a coincident stop event is recorded. It is not expected that this option will be typically used, and it exists principally as a hedge against failures of the TOF system.

4.2.2. *Over Counting and Auto Shutdown*

The basic strategy involves monitoring the start and stop singles rates. If these exceed a programmable threshold, shutdown is conducted as follows: the CPR potential is reduced. If over-counting continues, it is reduced further, until over-counting ceases to exceed the threshold or the supply is disabled. Then the Optics bias is reduced or shut down in the same way. Only then are the MCP biases reduced or shut down if necessary to remove the over-counting condition. Other anomalous conditions are also detected and result in a spectrum of corrective measures, culminating in shut down and manual restart.

4.2.3. *Steering Controller*

Heavy ion, neutral oxygen, data will likely be taken in two modes. The first mode, known as ‘enhanced efficiency mode’, results because neutral oxygen hitting the tungsten surfaces produces not only converted negative ions but also sputtered hydrogen. This sputtered hydrogen contribution will increase the LENA efficiency for oxygen by up to a factor of two in some cases. This mode, however, requires the separation of the signal due to converted atomic hydrogen (hydrogen does not sputter a significant amount of oxygen from the tungsten surfaces) from that due to sputtered hydrogen from the atomic oxygen.

The second mode, known as ‘sputter suppression mode’, relies on the ability of the steering controller to eliminate the low-energy sputtered hydrogen component from the higher energy converted atomic oxygen component. In this mode, none of the hydrogen part of the time-of-flight section is due to oxygen, and the neutral

LENA Science Data Flow

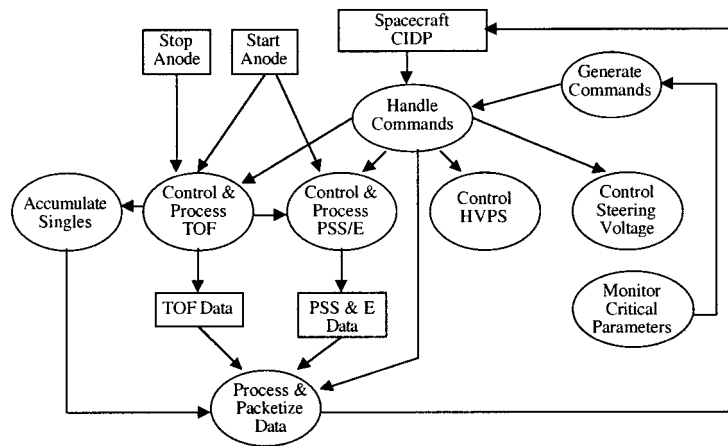


Figure 14. Data flow chart.

hydrogen fluxes may be determined without relying on subtracting the contribution due to sputtered hydrogen from the incident neutral oxygen.

Finally, calibration data show that the steering controller can also be successfully employed to eliminate the low energy parts of the distribution. For example, a steering controller setting of 31% maximum will eliminate 30 eV neutral oxygen. A steering controller setting of 50% maximum will eliminate 60 eV neutral oxygen. And so forth, although at the highest energies the flux is only reduced, not eliminated. This behavior, independent of the energy binning, may be used to infer additional information on the energy distribution of neutral atoms in much the same way the a retarding potential analyzer (RPA) functions.

4.3. DATA REPORTING OPTIONS

The remaining options for operation of LENA fall in the category of data options. The flow of data within LENA is summarized in Figure 14. Since onboard processing requirements are modest, and the CIDP is available for compression operations, there is little need for buffering of the data, and events are accumulated directly into image bins as they are accumulated in memory.

4.3.1. Scientific Data Types

The LENA ITOF system produces four principal types of data products that are accumulated separately and buffered in the CIDP for introduction into the IMAGE telemetry stream (see also Table III):

(1) Detector pulse 'singles' rates corresponding to the start, stop, and coincidence rates, without regard to position sensing.

TABLE III
Summary of LENA data products

LENA Data Product	Explanation
Start singles rate	Rate of all start events by Az
Stop singles rate	Rate of all stop events by Az
Coincidence singles rate	Rate of coincidence events
Direct events	16 bit representation of M, E, P, Az for each coincidence event (less M for start-only events).
Region of interest spectra	TOF spectrum for, integrated over a specified range of E, P
Image data	Array of $2M \times 3E \times 12P \times 45Az$

(2) ‘Direct Events’ or start/stop coincidence pairs are accumulated into a memory that retains all of the information about each event: TOF, energy and angle positions, and spin phase. Each direct event is stored as 16 bits (10 bits of TOF information, 4 bits of polar zone information, and 2 bits of energy information). TOF information is initially stored in 11 bits providing 2048 possible bins within the TOF range of response, but only the 10 most significant bits are included in the Direct Event data packet.

(3) ‘Region of Interest Spectra’ are TOF spectra accumulated from a specified subset (or the entirety) of the images. A TOF spectrum is accumulated for a specified range of polar angle and energy. This spectrum is divided into 32 bins based on a given TOF start/stop range. The subset of the image may be any contiguous rectangular subset of the full image data. The subset of the image may be any contiguous rectangular subset of the full image data.

(4) ‘Image data’, or coincidence pairs are accumulated into an array of accumulators corresponding to 2 commandable TOF ranges (corresponding to the major species of interest), 3 E/q bins, 12 polar-angle bins, and 45 spin azimuth bins. Start-only data may optionally be binned in the same way.

4.3.2. Bulk Data Compression

Arrays of data are further compressed by the IMAGE spacecraft CIDP, using a lossless encoding technique similar to those used for telecommunications of computer files. This eliminates redundant information and provides reductions in the total data volume by a factor ranging from approximately 2 to several, depending on the information content of the specific data. The resulting data volume depends in general upon the nature of the data collected, but this uncertainty is handled by buffering with direct events up to the capacity of the remaining telemetry space.

TABLE IV
LENA data product 'model' mix

LENA data product	'Model' volume
Housekeeping	64 bytes
Singles data	180 bytes
ROI spectra	64 bytes, for each of 4 defined regions
Image data	6480 bytes
Direct events	5760 bytes, maximum
Total stream	8000 bytes \times compression factor

Without compression, the LENA data bandwidth is just sufficient to report all image data plus a modest amount of TOF spectral data, and small amount of direct event data. With compression operational, the available telemetry bandwidth exceeds the LENA requirements to report images. To take advantage of this additional bandwidth, direct event data will be introduced as needed to fill the available telemetry buffers. Because the event data may be truncated, it is organized and reported in such a way as to provide an even distribution across spin azimuth. The data are reported in order of increasing spin sector bin, but the flight software will maintain a maximum limit of 128 bytes of event data per spin sector which will prevent only a few spin sector bins from filling the available telemetry space. In this way, more detailed information will become available as a benefit of the lossless compression processing. The direct event data so-obtained will be used to develop a more detailed understanding of the LENA efficiencies and in-flight performance.

4.4. SCIENCE OPERATIONS

LENA Science Operations will consist primarily of achieving operational high voltages, and the selection of the mix of the various products to be included in the telemetry stream. After experience is gained with LENA, a regular pattern may be established of modulating the steering voltage so as to obtain data with and without sputtering suppressed. The principal variable in the data selection is the amount of space to be devoted to ROI spectra, up to 4 of which can be defined and included in the telemetry stream. The balance is then devoted to direct events. The 'model' data product mix is summarized in Table IV.

The most scientifically important data products will initially be the LENA atom flux images, an example of which is shown in Figure 15, which has been generated using the calibrated instrument response to a flux image generated by a simulation model. Here the total flux of both O and H is summed and the instrument response is the non-mass resolved

The model used to produce these images included ENA produced by upflowing ions from the cleft ion fountain, the auroral zone and the polar cap as well as backplash ENA produced by precipitating ring current O^+ . The assumptions and characteristics of the model are:

(1) The model assumes that the flux of ions coming from the ionosphere is proportional to the energy flux carried by precipitating electrons as given by the (Hardy et al., 1987) empirical model.

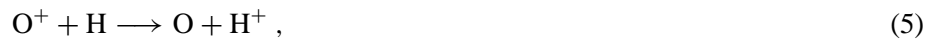
(2) The total flux of O^+ and H^+ ions coming from the ionosphere is consistent with the results of (Yau et al., 1988), (Pollock et al., 1990) and (Giles et al., 1994).

(3) A solution is found by launching many ions from the 1000 km source altitude and tracking them as they follow field lines, drifting due to the convection electric field and losing energy to gravity. This is done with a guiding center particle trajectory code (Delcourt et al., 1988).

(4) The ions begin life (at 1000 km) having velocities drawn from a perpendicularly heated biMaxwellian distribution whose perpendicular temperature is 10 times its parallel temperature. In the auroral zone the perpendicular temperature of this distribution is 30 eV in the cleft ion fountain it is 10 eV and in the polar cap it is 20 eV.

(5) The magnetic field is assumed to be dipolar and the convection electric field model is that of (Volland et al., 1978).

(6) The following charge exchange reactions are included in the model. The neutral atmosphere used is that given by the MSIS-86 model and the ionospheric O^+ is that given by the IRI-90 model.



(7) The solution found is steady state and depends mainly on Kp and $F10.7$ as given by the total outflow fluxes of (Yau et al., 1988).

Images like that in Figure 15, coming at intervals of a few spins of the IMAGE spacecraft, will allow coarse spatial resolution monitoring of auroral plasma heating with unprecedented time resolution. The advantage of having this time resolution will be to correlate the heating with external influences so that the cause of the heating can be tracked to its energy sources. Because the times-of-flight of the observed atoms from their source regions are quite long for the lowest energy atoms observable to LENA (up to 10 min per R_E), the correlation of plasma heating with other solar wind or magnetospheric phenomena will require careful timing

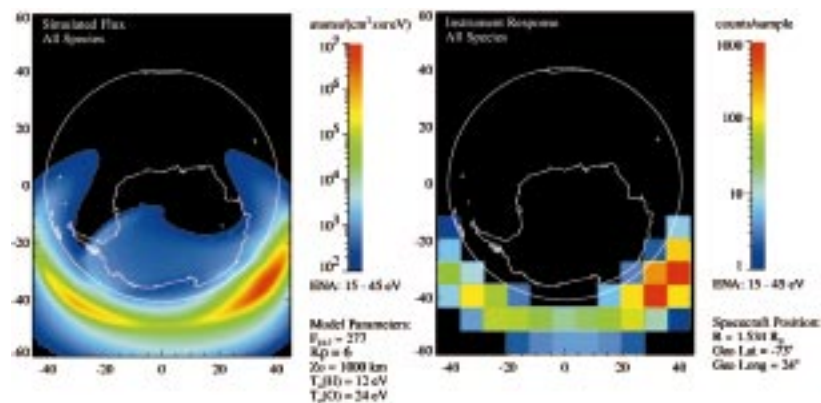


Figure 15. Example of predicted LENA response to neutral atom fluxes computed to be emitted by the auroral oval under conditions of active aurora.

with regard to both the delivery of energy to the auroral zone as well as the subsequent travel of atoms to the IMAGE spacecraft. Moreover, at these lower energies, there will be noticeable gravitational deflections of the neutral atom trajectories, leading to some distortion and smearing that will complicate the interpretation of the images.

5. Summary

The low-energy neutral atom (LENA) Imager has been developed to extend the goals of the neutral atom imaging to the lowest possible energy range, so that plasma heating and planetary escape can be remotely sensed and tracked at much higher than usual time resolution. LENA is the first such instrument to be flown in space. For this initial application, a conversion surface technology has been employed that may have a finite lifetime on orbit. There is little previous experience with charge state conversion by surfaces exposed for long periods to space vacuum levels, a situation that LENA will alleviate.

With nearly a full three dimensional view of the sky each spin, LENA's 12 angular pixels monitor two mass species and three energy ranges simultaneously, obviating the need to sweep any measurement parameter. The LENA C&DH accumulates images and TOF spectra (optionally for a subset of the imaged field of view). The image data routinely undergo lossless compression by the IMAGE spacecraft CIDP, to optimize telemetry use. As compression frees up telemetry space, it is filled with direct events that provide a continuous monitor of the TOF spectrum at higher resolution and allowing routine monitoring of minor species that may be of interest.

LENA will make possible for the first time global remote sensing of the heating and escape of ionospheric plasma into the magnetosphere, at a time resolution of

a few minutes, far faster than for previous in situ sampling of this process. It will also provide the first opportunity to observe other heliospheric fluxes of fast neutral atoms, potentially from the interstellar medium, the sun, or planets and other solar system bodies.

Appendix A. Low-Energy Neutral Conversion

The rationale behind using the surface conversion of neutral atoms to negative ions for the LENA instrument has been discussed briefly in the introduction section. This technology is the most developmental aspect of the LENA instrument, and clearly is fundamental to its operation. Meaningful evaluation of data from LENA depends upon three features of the conversion process:

- Approximately specular reflection of the incident particles.
- A temporally stable, calibrated conversion efficiency.
- A predictable energy relationship between the incident neutrals and the negative ions.

Most of what is known about this process is empirical, with only limited theoretical basis. Much of the existing work is summarized by (Gruntman, 1997). The majority of previous measurements of the conversion efficiencies for various surfaces have been devoted to H and D, atoms important to fusion processes. Moreover, some controversy surrounds the empirical results.

The efficiency for the conversion of neutral atoms incident on a surface to negative ions should ideally be a straightforward measurement. The conversion efficiency, often denoted by the symbol η , is simply the ratio of the near-specularly-reflected flux of negative ions, A^- , from a surface to that of the incident neutral flux, A_{inc} :

$$\eta = \frac{A^-}{A_{\text{inc}}} . \quad (7)$$

In some of the relevant literature, a different figure of merit called the ‘ionization efficiency’ or ‘ion fraction’ is used. This measurement is the ratio of the detected negative ions reflected from the surface to the sum of the detected ions and neutrals reflected from the surface. The use of this parameter may produce some confusion regarding the performance of the surfaces and is responsible in part for the controversy. The important parameter for neutral atom imaging is clearly the conversion efficiency, and we use that exclusively herein.

The conversion efficiency should depend upon many experimental parameters: the angle of incidence, the incident neutral species, the neutral energy, and the material and preparation of the conversion surface. There have been measurements investigating the effect of these parameters reported in the literature. The formation of H^- by hyperthermal H atoms backscattered from a thick cesium surface was studied by Pargellis and Seidl (1982). The scattering of fast (70 eV to 1 keV)

neutral and ionic molecular hydrogen from an Ag(111) surface was studied extensively by van Slooten et al. (1992). In addition, scattering of 80–300 eV O₂ and NO from Ag(111) and Pt(111) was studied by Reijnen, Van Slooten and Kleyn (1991). The results of these neutral beam experiments have an impact upon the perceived applicability of studies accomplished with ionic beams, which will be illuminated in the next paragraph. The majority of previous studies have used incident beams of atomic or molecular ions and the results have been extrapolated to the case of incident neutral atoms. According to theory (Probst and Luescher, 1986; Snowdon et al., 1986), and strong experimental evidence (Schneider et al., 1982; Van Toledo, 1986; Wurz et al., 1998), the charge state of the reflected atom is independent of its incident charge state. This results because the incoming ions are neutralized by an Auger-type electron transfer process or by resonant electron transition. As a result, measurements of the ionization efficiency using beams of positive molecules or atoms are represented as an adequate method of determining the conversion efficiency. Nevertheless, the LENA team was the first to directly measure the absolute conversion efficiencies of neutral atoms to negative ions on surfaces using calibrated beams of variable-energy neutrals incident upon surfaces.

In reality, neutral to negative ion conversion measurements are inherently complicated. Perhaps the most daunting problem is the production of a well-calibrated, variable energy beam of neutral atoms. Many measurements have been used to infer the conversion efficiencies for various surfaces. Most of these measurements depend upon one or more of the following aspects, leading to some controversy about their applicability:

(1) The use of positively charged particles for the incident beam. There is a strong heritage in the literature that maintains that conversion efficiencies should not depend upon the incident charge state. This dependence has not been investigated in detail. However, Van Slooten et al. (1992) have shown that energy distributions and angular dependence of negative (as well as positive) ions resulting from neutral molecular hydrogen incident upon Ag(111) markedly differ from those for incident positive ions.

(2) The use of molecules for the incident beam. The use of incident molecular beams additionally demands that assumptions be made about the rate of and energy dependence of dissociation upon the surface. Two problems may arise with the use of molecular beams. The first is that there may be avenues to produce negative atoms from a molecule that are not available to the atom. The second is that unless mass analysis (or careful energy analysis) is used to examine the reflected negative ions, molecular negative ions that are formed in the scattering process may influence the results. Reijnen et al. (1991) observed very strong signals of O₂⁻ resulting from O₂ incident upon Ag(111) and Pt(111) at energies from 80–300 eV.

(3) A lack of energy analysis of the reflected neutral and ionic particles. Unless the ion and neutral flux (in the case of charge fraction measurements) are energy analyzed and detected on a calibrated detector, the results may be considered suspect, owing to known detection efficiency variations with energy.

(4) Requirement for atomically clean surfaces. Many of the previous results are for atomically clean surfaces, which are exceedingly difficult to produce and maintain in a space flight instrument.

The goal of the study of possible surfaces for LENA was to use previous work as a guide and pursue a course of research leading to an acceptable conversion surface suitable for operation aboard a satellite. The necessary requirements included durability, long term stability, uniform and predictable conversion efficiency, and realistic demands upon the spacecraft power systems. Although the literature suggested that there might be several promising methods of converting neutral H and O to negative ions, there was no data that could be used outright for the determination of the proper surface to use in space. Initial investigations focussed on matching the electron affinities of H and O with the electron binding energy of a proposed surface in the hopes of achieving a quasi-resonant electron transfer resulting in the conversion of the neutrals to negative ions. The electron affinity of H is 0.75 eV and the electron affinity of O is 1.46 eV, consequently a search for a possible conversion surface with an electron binding energy in this range was undertaken. The most promising candidate appeared to be that of cesiated tungsten. This was suggested by earlier work of Van Toledo (1986). These studies showed ionization efficiencies of >10% were possible using atomically clean, crystalline tungsten surfaces covered with ~ 1 monolayer of cesium. Although both of these measurements were accomplished using incident beams of positive ions, together they provided a compelling argument for pursuing cesiated surfaces for use in LENA.

The University of Denver and the University of Bern investigated possible surfaces for the conversion of neutral atoms to negative ions for use on LENA. The University of Bern was better equipped to investigate thermal methods of preparing a tungsten substrate prior to cesiation and to determine the angular reflection characteristics of the converted ions. Although the University of Bern used an incident beam of H_2^+ or O_2^+ , comparisons of angular scattering results with those of the University of Denver bolstered confidence in the applicability of the results. The laboratory at the University of Denver (described in the body of this article) used calibrated beams of O and H neutrals and was responsible for the measurements of the conversion efficiencies of the surfaces, as well as serving as a calibration facility for the spacecraft instrument.

A major research thrust of the LENA team was the investigation of cesiated tungsten surfaces for use as conversion surfaces. This research involved the preparation and characterization of these surfaces. It is well known that laboratory surfaces are covered with a layer of physisorbed and chemisorbed molecules. In order to establish a clean surface of substrate material or a smooth deposited layer of cesium; the surface must first be cleaned in vacuum. Cleaning procedures were evaluated at the University of Bern. By examining work function of the resulting surface, it was determined that heating a tungsten substrate to 800 °C for two minutes was a minimum requirement for a clean substrate suitable for cesium

Retarding Potential Analysis of Converted Neutrals

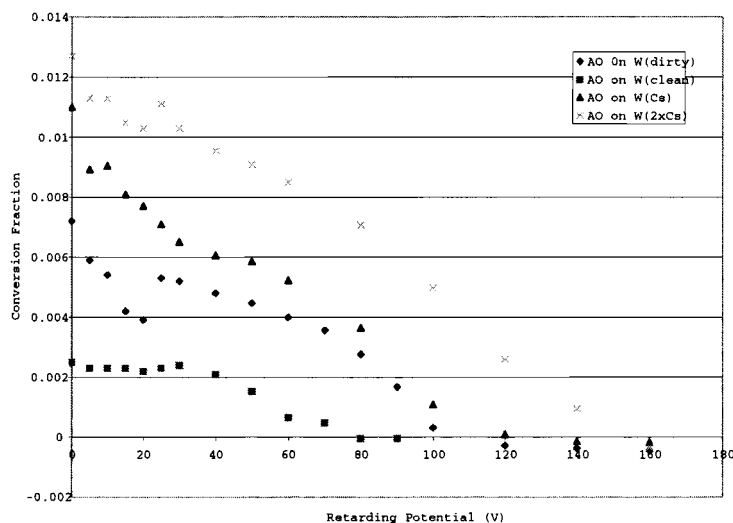


Figure 16. Summary of RPA analysis data for atomic atom conversion to negative ions on bare polycrystalline tungsten, adsorbate-coated tungsten, and cesiated tungsten.

deposition. Cesium was then deposited upon the surface after it cooled to below 300 °C. Any surface will readsorb molecules from the vacuum at a rate depending upon the pressure in the chamber and the sticking coefficients for the various molecules comprising that pressure (usually water-dominated). The cesiated surface will then be rendered ineffective by these new adsorbates. The heating and deposition process can then be used to rejuvenate the surface (Aellig et al., 1998). However, delaying the degradation of the cesiated surface by days would require an operational pressure inside the instrument of $\sim 10^{-9}$ Torr. Operation at such pressures within instruments on orbit, to say nothing of laboratory calibration conditions, would require a high temperature bake-out and extremely careful attention to materials.

It was found in testing, at pressures in the mid- 10^{-8} Torr range, that the cesiated surfaces had lifetimes of only about 30 minutes. Additionally the freshly cesiated surfaces only offered an approximate factor of two advantage over untreated laboratory surfaces in the conversion of H and O to negative ions (2% vs 1%, as shown in Figure 16). On the basis of this information, cesiation was abandoned as a conversion surface technology, in favor of the use of laboratory surfaces, presumably covered mainly with layers of polar (water) molecules that naturally occur in vacuum chambers and instruments. Consideration was given to the provision of a steady source of such volatiles within the instrument, but it was ultimately decided that normal outgassing of materials would likely provide an adequate source, and that the final monolayers would be difficult to remove in any case. A major concern was that EUV exposure of the surface would lead to a clean surface with a reduced conversion efficiency, but testing with a source similar in magnitude to

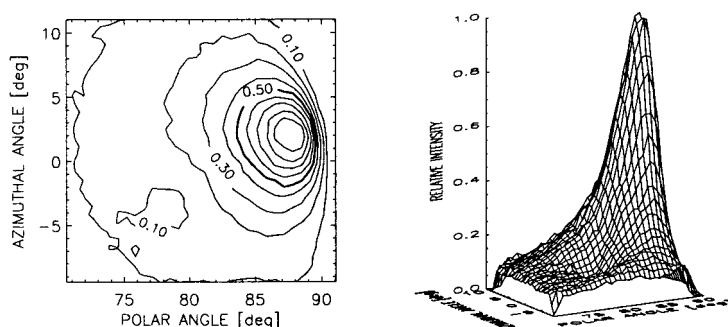


Figure 17. Reflection pattern for conversion of incident ions upon polycrystalline tungsten, with monolayer coating of residual vacuum adsorbates. This pattern is characteristic of results expected from the LENA conversion surface.

the solar EUV spectrum showed that there was no discernable reduction in surface conversion efficiency.

It is possible that other materials exist that have a superior conversion efficiency and that are more stable than cesiated surfaces against surface contamination, in particular oxidation. However, such surfaces will also be rapidly coated with adsorbates in any real instrument in the laboratory or on orbit, possibly degrading the conversion surface until the volatiles are driven off. This has been observed in tests investigating several other possible conversion surfaces at the University of Denver, including polycrystalline diamond and barium zirconate coatings on tungsten. Unless the surfaces can be passivated against reaccumulation of adsorbates, it appears necessary to run such surfaces at elevated temperatures on a continuous basis to maintain superior conversion efficiencies. If such continuous heating can not be supported, it will be necessary to accept the conversion efficiency of surfaces coated in volatile adsorbates for routine operations, as we have done for LENA.

The conversion surface selected for LENA was thus polycrystalline tungsten, polished to a surface roughness less than 5 nm RMS. This polished surface, when clean, results in near-specular reflection of the converted neutrals. This characteristic of the reflected ions is only slightly degraded for a surface coated with ~ 1 monolayer of cesium or volatiles adsorbed from the vacuum, as shown in Figure 17. The reflected ions are reflected with several degrees of dispersion around the specular direction. The dispersion is moderately wider and is asymmetric in the polar angle as compared to the azimuthal angle (relative to surface normal), and decreases as the polar angle of incidence (measured from the normal) becomes larger. This dispersion is overcome by the LENA IXL focussing in the polar angle direction. The polar dispersion leads to a limit on the polar angle resolution of LENA, effectively broadening any particular pencil of incident neutral particles. This effect is reduced by higher accelerating potentials in the IXL. The design goal of 8-deg resolution is met for an incident energy < 1 keV, and an accelerating potential of 15 to 20 kV. Negative ions resulting from the conversion of incident neutral

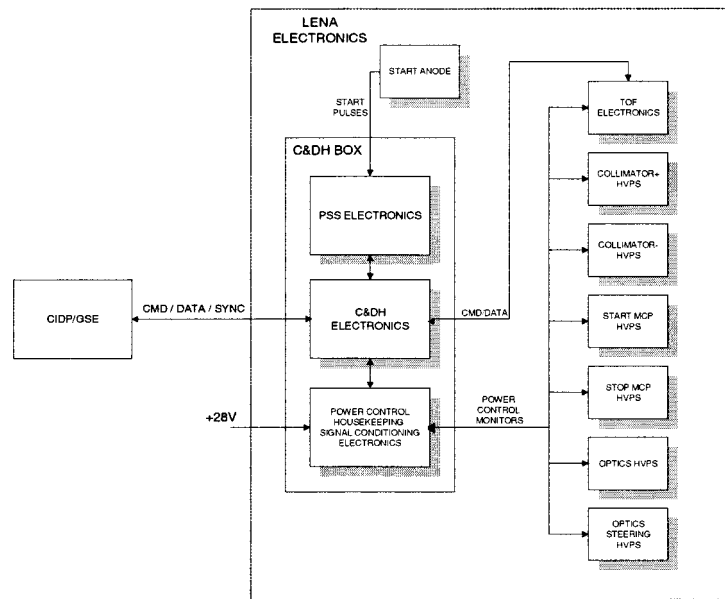


Figure 18. LENA simplified electronics functional block diagram.

atoms retain a characteristic energy distribution ($E \sim 60\%$ of the incident energy for O and 80% for H) that can be used to determine the energy distribution of the incident atomic flux. Possible false signals could arrive from ions, particularly H^- , produced by sputtering of water constituents by incident O atoms. These ions were observed during calibration but resulted only from incident O atoms, not from H atoms incident. These sputtered ions are at very low energy (a few eV) and can be easily discriminated, as described in the response section of this paper.

Appendix B. Electronics Description

The major LENA electronics subsystems are: spacecraft power and data interfaces; low voltage power supplies and filters (± 3 , ± 5 , ± 10 , ± 15 , and 28 V); high voltage power (0 to 3.0 kV for start and stop MCPs, 0 to ± 8 kV, 0 to -20 kV), TOF electronics, C&DH and associated logic, and Ground Support Equipment (GSE). These functions are illustrated in Figure 18. The LENA electronics functions are divided among electronics board/boxes, as briefly summarized in Table V.

B1. COMMAND AND DATA HANDLING UNIT (C&DH)

The LENA C&DH is distributed among 2 processors: a UT69RH051 microcontroller (an 8051 variant) and an RH1280 FPGA (Figure 19).

The microcontroller provides a flexible platform for instrument development and operation. It lacks the ability however to respond to repetitive high speed

TABLE V
Electronics box/board functions

Box/board	Function
Start MCP box	0 to 3.0 kV HVPS
Stop MCP box	0 to 3.0 kV HVPS
CPR positive box	0 to 8.0 kV HVPS
CPR negative box	0 to -8.0 kV HVPS
Optics HVPS box	0 to -20 kV HVPS
C&DH box:	
C&DH/PSS board	Command and data handling, position sensing
Power control	± 5 , ± 15 , $+30$ analog signal conditioning, housekeeping
Mother board	integrates C&DH/PSS board and power control board, interfaces to CIDP

events. This capability is provided by the FPGA. These coprocessors communicate via memory mapped registers, digital I/O lines and interrupts.

The LENA basis science program is stored in an $8k \times 8$ PROM. A more comprehensive program that supports the full complement of LENA data products and autonomous operations capabilities is autonomously downloaded from CIDP EEPROM into the LENA $32k \times 8$ program-RAM after the basic program has booted. Program execution then proceeds from this memory space.

The 8051 provides 3 primary functions:

- configure instrument subsystems based on commands transmitted from CIDP,
- process and transmit science and housekeeping data in accordance with the configuration,
- monitor the instrument for undesirable behavior and initiate actions to correct it.

Commands are routed to LENA via an RS-422 interface at 38.4 kbaud. Handshaking is not implemented. Critical LENA commands are executed immediately. Other commands are queued and executed within several seconds.

Data are transferred to CIDP using the same specification. Up to 32 kB of science and housekeeping data are transferred during each spin cycle. Dual accumulation buffers are implemented for each data product, thereby permitting concurrent data acquisition and transmission.

The 8051 resident program incorporates modules that continually monitor instrument parameters to identify anomalous operation and potentially damaging conditions. If such conditions are detected, the instrument is autonomously recon-

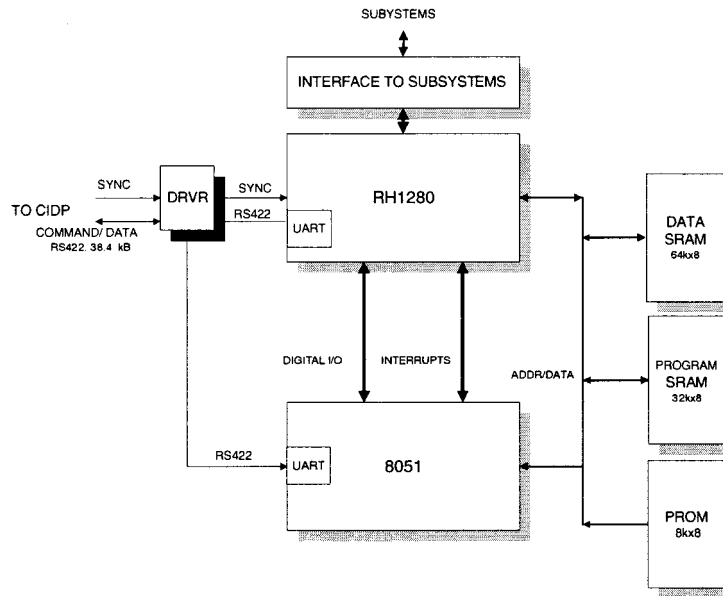


Figure 19. LENA C&DH dual processor architecture

figured in an attempt to return it to a desired region of operation. The C&DH also incorporates a watchdog timer to reset the CPU if program execution proceeds errantly. After the system has been reset it will attempt to return to a previously configured state and resume normal science operation.

The monitor modules also execute a comprehensive instrument self-test. The operational-space of the high voltage power supplies, TOF system and data processing modules is exercised. The self-test module then determines whether the subsystem has passed or failed the test by comparing observed and expected behavior. Including this capability in the flight software provides a thorough, repeatable and reliable method of verifying instrument operation.

The overarching goal is to give the instrument the ability to test itself and to return to a desired state if perturbed. These autonomous capabilities are critical since the 'lights-out' mode of IMAGE operations implies there may be significant latency between the onset of an anomalous condition and when the instrument can be manually reconfigured to address it. Since reactions are derived from onboard rules in addition to ground commands, potentially damaging conditions are handled more quickly and corrective actions are more comprehensive.

B2. HIGH VOLTAGE POWER SUPPLIES

LENA incorporates five high voltage power supplies that are attached to the exterior of the sensor, as summarized in Table VI. High voltage connections are made when a supply is mounted onto the sensor, using custom high voltage feedthroughs

that are incorporated into the power supply housing. Each supply receives power and control from the C&DH subsystem. Features common to all high voltage power supplies include:

- Digital commands include enable/disable, and a safe mode, where the output voltage is limited to one tenth of the normal maximum.
- The output voltage is controlled by an analog input from 0 to +10 V.
- Housekeeping monitors for HV output and input current have analog outputs with a range from 0 to +10 V. (The optics power supply also has a monitor for output current.)
- The safe mode is active for about 0.3 seconds after +30 volt power is turned on, so that the command inputs can stabilize. The safe mode is active when +30 V is supplied. An UNSAFE command must be executed to exit this mode.

The charged particle rejector power supplies (referred to as collimator supplies earlier in the development of the instrument) provide positive and negative high voltages to a set of parallel vanes with alternating polarities. Electrons and ions with energy-per-charge less than 100 keV e^{-1} are deflected, but neutral particles are permitted to enter LENA.

The optics high voltage power supply provides voltage for the conversion surface, and through a chain of resistors, the voltages used by the ion extraction lens and the electrostatic analyzer.

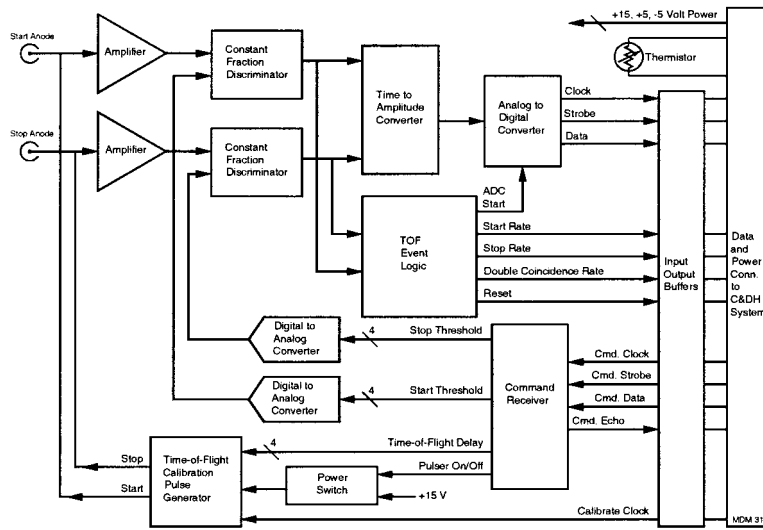
The microchannel plate power supplies provide all the high voltages needed in the time-of-flight analyzer. In addition to bias voltages for the MCPs, this includes a negative potential for the carbon foil, and the potential used on the mirror harp. The start and stop MCPs are operated from separate HVPS. In order to avoid the need for individual high voltage bias supplies for each sector, the MCPs have been specified to have consistent impedances from plate to plate. The four trapezoid start MCPs represent a load of 114 mW to the start supply, and the four rectangular stop MCPs, which have larger area, represent a load of 73 mW to the stop supply. Due to the consistency of MCP impedances, it was not necessary to use a center tap voltage in the chevron stack (an unused HVPS output was reserved for this). A negatively biased grid is used in front of the MCPs to increase their efficiency by trapping secondary electrons emitted from the front surface. MCP chevron stacks are chosen for consistent multiplication gains. During calibration, the optimum MCP bias operating points for start and stop detectors is determined by varying the biases and observing the integral rate of discriminated pulses.

B3. TIME-OF-FLIGHT ELECTRONICS

The time-of-flight (TOF) electronics is a self-contained subsystem mounted on the LENA sensor housing. A pair of Nanohex connectors brings the start and stop microchannel plate pulses in from the sensor. A 31-pin MDM connector is used for power input and data communications. Figure 20 shows a block diagram of the LENA TOF electronics.

TABLE VI
LENA high voltage power supply specifications

HVPS Name	Maximum output	Load	Ripple (p-p)	HV outputs	HK monitor outputs
Charged particle Rejector, positive	+8.8 kV	≥880 MW	≤0.05%	1	I (input) V (output)
Charged particle Rejector, negative	-8.8 kV	≥880 MW	≤0.05%	1	I (input) V (output)
Optics	-22.0 kV	5000 MW	≤0.1%	1	I (input) I (output) V (output)
MCP bias, start	+3.0 kV	114 MW	≤0.1%	5	I (input) V (output)
MCP bias, stop	+3.0 kV	73 MW	≤0.1%	5	I (input) V (output)



LENA TOF ELECTRONICS BLOCK DIAGRAM

Figure 20. LENA TOF electronics block diagram

The start or stop microchannel plate pulse enters a two-stage amplifier with 50 ohm input impedance. The output of this amplifier is sent to a constant-fraction timing discriminator (CFD) with amplitude discrimination. The amplitude discriminator level is adjustable from less than 10 mV to 50 mV, in 15 linear steps. If the microchannel plate signal amplitude is above this level, a logic pulse generated by the timing discriminator is sent to the time-to-amplitude-converter (TAC) circuit, and to the TOF logic. Input pulse amplitude variations result in less than 1 nanosecond of walk in the TOF measurement (changing both start and stop inputs over the range from 10 to 1000 mV).

The TAC circuit produces an output pulse with an amplitude that is proportional to the time difference between the start and stop input pulses, over a range from 5 to 303 ns. It is implemented by charging a capacitor with a constant-current source during the time interval between a start input and the next stop input. An analysis window, which defines the minimum and maximum TOF, opens 5 ns, and closes 319 ns, after a start pulse is detected. If there is no stop pulse within the analysis window, the TAC circuit is reset, and the dead time is about 1 μ s.

If there is a stop pulse within the analysis window, a double coincidence rate (DCR) pulse is produced. This starts the analog to digital converter (ADC) measurement of the TAC output. The 14-bit ADC used includes a track and hold amplifier at the input, and a serial interface output that communicates directly with the C&DH subsystem. While all 14 bits are sent to the C&DH, only the 8 most significant bits are included in telemetered direct events. The dead time, when an event is processed, is about 13 μ s.

In addition to the time-of-flight data, there are three types of pulses sent to the C&DH subsystem for rate measurements: start, stop and double coincidence. A start or stop singles rate pulse is generated whenever an event triggers the start or stop discriminator. As mentioned previously, a DCR pulse is generated whenever the stop discriminator is triggered while the analysis window is open. Dead time for the DCR pulse is 1.6 μ s.

An internal time-of-flight calibration pulse generator may be turned on for testing as required. It produces a pulse to the start amplifier, followed by one to the stop amplifier after a delay (of 20, 40, 60, up to 300 ns) that is selected by command. A clock from the C&DH unit controls the repetition rate. To save power, this built in test pulse generator is turned off when not in use.

Commands are received from the C&DH unit over a 16-bit serial interface, and are echoed back for verification. The start and stop discriminator thresholds are individually adjustable with 4-bit levels. Another 4-bits are used to control the time-of-flight delay of the built in test pulse generator, and one bit is used to turn the generator on or off.

Acknowledgements

The authors acknowledge the vital contributions of John Annen, Robert Calvo, Mike Choi, Bernard Fridovich, Cheyenne Harris, Ken Harris, Charles He, Floyd Hunsaker, Jennifer Kalb, Diane Kolos, Evelyn Lee, Henning Leidecker, George Miller, Kevin Milligan, Kim Moats, Bert Nahory, Frank Ottens, John Park, Jeff Pattison, Frank Shaffer, Wayne Shanks, Rajeev Sharma, Sandy Shuman, Carol Tedore, Tim Van Sant, Richard Vondrak, Maxine Windhausen, and the environmental test staff at GSFC. LMATC work was carried out under NASA contract NAS5-97211 and SwRI contract 83815. UMD work was supported by SwRI contract 83821. Work at the University of Denver was supported by NASA contract NAG5-3386. Work performed at Univ. of Bern was funded by the Swiss National Science Foundation. The continuous support of this project by Peter Bochsler of the University of Bern is gratefully acknowledged.

References

- Aellig, M. R., et al.: 1998, 'Surface Ionization with Cesium Converters for Space Applications', *Geophysical Monograph 103*, Am. Geophys. Un., Washington, DC, p. 289.
- Collin, H. L., Peterson, W. K., Lennartsson, O. W. and Drake, J. F.: 1998, 'The Seasonal Variation of Auroral Ion Beams', *Geophys. Res. Lett.* **25**(21), 4071.
- Dahl, D.: 1995, SIMION 3D 6.0, pub. # INEL-95/0403, Idaho National Engineering Laboratory, Chemical Materials and Process Department, Lockheed Idaho Technologies Co., Idaho Falls, ID.
- Delcourt, D. C., et al.: 1988, 'Influence of the Interplanetary Magnetic Field Orientation on Polar Cap Ion Trajectories: Energy Gain and Drift Effects', *J. Geophys. Res.* **93**, 7565.
- Fasola, J.: 1977, 'H- Source Development at ANL', *IEEE Trans. Nucl. Sci.* **NS-24**, 1597.
- Ghielmetti, A. G., Shelley, E. G., Fuselier, S., Wurz, P., Bochsler, P., Herrero, F., Smith, M. F. and Stephen, T. S.: 1994, 'Mass Spectrograph for Imaging Low-Energy Atoms', *Opt. Eng.* **33**, 362.
- Giles, B. L., et al.: 1994, 'Statistical Survey of Pitch Angle Distributions in Core (0–50 eV) Ions from Dynamics Explorer 1: Outflow in the Auroral Zone, Polar Cap, and Cusp', *J. Geophys. Res.* **99**, 17483.
- Gloeckler, G. and Hsieh, K. C.: 1979, 'Time-Of-Flight Technique for Particle Identification at Energies from 2–400 keV/Nucleon', *Nucl. Instr. Meth.* **165**, 537.
- Gruntman, M.: 1992, 'A New Technique for *in situ* Measurement of the Composition of Neutral Gas in Interplanetary Space', *Planetary Space Sci.* **41**(4), 307.
- Gruntman, M.: 'Energetic Neutral Atom Imaging of Space Plasmas', *Rev. Sci. Instrum.* **68**(10), 3617.
- Hardy, D. A., et al.: 1987, 'Statistical and Functional Representation of the Pattern of Auroral Energy Flux, Number Flux, and Conductivity', *J. Geophys. Res.* **92**, 12275.
- Herrero, F. A. and Smith, N. F.: 1992, 'Imager of Low Energy Neutral Atoms (ILENA): Imaging Neutral Atoms from the Magnetosphere at Energies Below 20 keV', *Instrumentation for Magnetospheric Imagery*, SPIE pub. # 1,744, pp. 32–39.
- Moore, T. E. and Delcourt, D. C.: 1995, 'The Geopause', *Rev. Geophys.* **33**(2), 175.
- Moore, T. E., et al.: 1999, 'Ionospheric Mass Ejection Response to a CME', *Geophys. Res. Lett.* **26**(15), 1.
- Pargellis, A. and Seidl, M.: 1982, 'Formation of H⁻ Ions by Backscattering Thermal Hydrogen Atoms from a Cesium Surface', *Phys. Rev. B* **25**(7), 4356.

- Probst, F. M. and Luescher, E.: 1963, 'Auger Electron Ejection from Tungsten Surfaces by Low Energy Ions', *Phys. Rev.* **132**, 1037.
- Pollock, C. J., et al.: 1990, 'A Survey of Upwelling Ion Event Characteristics', *J. Geophys. Res.* **95**, 18969.
- Reijnen, P. H. F., van Slooten, U. and Kleyn, A. W.: 1991, 'Negative Ion Formation and Dissociation in Scattering of Fast O₂ and NO from Ag(111), and Pt(111)', *J. Chem. Phys.* **94**(1), 695.
- Roelof, E. C.: 1987, 'Energetic Neutral Atom Image of a Storm-Time Ring Current', *Geophys. Res. Lett.* **14**, 652.
- Schneider, P. J., Eckstein, W. and Verbeek, H.: 1982, 'Charge States of Reflected Particles for Grazing Incidence on D⁺, D₂⁺, and Do on Ni and Cs Targets', *Nucl. Instrum. Meth.* **194**, 387.
- Smith, M. F., et al.: 1998, 'Imaging Low-Energy (keV) Neutral Atoms: Ion-Optical Design', *Geophysical Monograph #103*, Am. Geophys. Un; Washington DC, p. 263.
- Snowdon, K. J., Willerding, B. and Heiland, W.: 1986, 'Molecule Excitation in Sputtering, Scattering, and Electron or Photon Induced Desorption', *Nucl. Instrum. Meth. B* **14**, 467.
- Stephen, T. M., Van Zyl, B. and Amme, R. C.: 1996, 'Generation of a Fast-Oxygen Beam from O⁻ Ions by Resonant Cavity Radiation', *Rev. Sci. Instrum.* **67**(4), 1478.
- Taglauer, E.: 1985, 'Investigation of the Local Atomic Arrangement on Surfaces Using Low-Energy Ion Scattering', *Appl. Phys. A* **38**, 161.
- Van Toledo, W.: 1986, 'Formation of Negative Hydrogen Ions on a Cesium Tungsten Surface and its Application to Plasma Physics', *Proc. of Production and Application of Light Negative Ions*, Laboratoire de Physique des Milieux Ionisés, École Polytechnique, Palaiseau, France, p. 193.
- Van Slooten, U., Andersson, D. R. and Kleyn, A. W.: 1992, 'Scattering of Fast Molecular Hydrogen from Ag(111)', *Surf. Sci.* **274**, 1.
- Volland, H.: 1978, 'A Model of the Magnetospheric Electric Convection Field', *J. Geophys. Res.* **83**, 2695.
- Walton, D. M., James, A. M., Bowles, J. A.: 1998, 'High Speed 2-D Imaging for Plasma Analyzers Using Wedge-and-Strip Anodes', *Measurement Techniques Space Plasmas: Particles*, *Geophysical Monograph #102*, AGU, Washington, DC, p. 295.
- Wurz, P., Bochsler, P., Ghielmetti, A. G., Shelley, E. G., Herrero, F. and Smith, M. F.: 1993, 'Concept for the HI-LITE Neutral Atom Imaging Instrument', in P. Varga and G. Betz (eds), *Proceedings of Symposium on Surface Science*, Kaprun, Austria, p. 225.
- Wurz, P., Aellig, M. R., Bochsler, P., Ghielmetti, A. G., Shelley, E. G., Fuselier, S. A., Herrero, F., Smith, M. F., Stephen, T. S.: 1995, 'Neutral Atom Mass Spectrograph', *Opt. Eng.* **34**, 2365.
- Wurz, P., Frohlich, T., Brüning, K., Scheer, J., Heilourd, W., Hertzberg, E., Fuselier, S. A.: 1998, 'Formation of Negative Ions by Scattering from a Diamond (111) Surface', in J. Safrankova, and A. Koruka (eds), *Proc. of the week of doctoral students*, Charles University, Prague, Czech Republic, p. 257.
- Yau, A. W., et al.: 1988, 'Quantitative Parametrization of Energetic Ionospheric Ion Outflow', in Modeling Magnetospheric Plasma', T. E. Moore and J. H. Waite, Jr. (eds), *Geophys. Mono. #44*, AGU, Washington, DC, p. 211.